Lawrence Berkeley National Laboratory

Title
A Heavy Ion Spectrometer System for the Measurement of Projectile Fragmentation of Relativistic Heavy Ions

Permalink
https://escholarship.org/uc/item/5xs697tm

Author
Engelage, J.

Publication Date
1996-06-03

ERNEST ORLANDO LAWRENCE BERKELEY NATIONAL LABORATORY

A Heavy Ion Spectrometer System for the Measurement of Projectile Fragmentation of Relativistic Heavy Ions

J. Engelage, S. Albergo, Z. Caccia, C.-X. Chen, S. Costa,
H.J. Crawford, M. Cronqvist, I. Flores, R. Fonte,
L. Greiner, T.G. Guzik, A. Insolia, C.N. Knott, S. Ko,
C. Kuo, P.J. Lindstrom, J. Mazotta, M. McMahon,
J.W. Mitchell, R. Potenza, J. Romanski, G.V. Russo,
A. Soutoul, O. Testard, C.E. Tull, C. Tuvé,
C.J. Waddington, W.R. Webber, and J.P. Wefel
Nuclear Science Division

June 1996

DISCLAIMER

A Heavy Ion Spectrometer System for the Measurement of Projectile Fragmentation of Relativistic Heavy Ions

J. Engelage,[d] S. Albergo,[h] Z. Caccia,[h] C.-X. Chen,[c], S. Costa,[h]
H.J. Crawford,[d] M. Cronqvist,[b] I. Flores,[b] R. Fonte,[h] L. Greiner,[d] T.G. Guzik,[c]
A. Insolia,[h] C.N. Knott,[e] S. Ko,[d] C. Kuo,[d] P.J. Lindstrom,[b] J. Mazotta,[d]
M. McMahon,[c] J.W. Mitchell,[a] R. Potenza,[h] J. Romanski,[h] G.V. Russo,[h]
A. Soutoul,[g] O. Testard,[g] C.E. Tull,[c,l] C. Tuvé,[h] C.J. Waddington,[e]
W.R. Webber,[f] and J.P. Wefel[c]

(The TRANSPORT Collaboration)

[a]NASA/Goddard Space Flight Center, Greenbelt, MD, USA
[b]Ernest Orlando Lawrence Berkeley National Laboratory, University of
 California, Berkeley, CA 94720, USA
[c]Louisiana State University, Baton Rouge, LA, USA
[d]Space Sciences Laboratory, University of California, Berkeley, CA 94720, USA
[e]University of Minnesota, Minneapolis, MN, USA
[f]University of New Mexico, Las Cruces, NM, USA
[g]Service d'Astrophysique, C.E.N. Saclay, Cedex, France
[h]Universitá di Catania, INFN, Sezione di Catania and CSFNSM, Catania, Italy
[l]Current address: Ernest Orlando Lawrence Berkeley National Laboratory,
 University of California, Berkeley, CA 94720, USA

June 1996

A Heavy Ion Spectrometer System for the Measurement of Projectile Fragmentation of Relativistic Heavy Ions

J. Engelage[d], S. Albergo[h], Z. Caccia[h], C.-X. Chen[c], S. Costa[h],
H.J. Crawford[d], M. Cronqvist[b], I. Flores[b], R. Fonte[h], L. Greiner[d],
T.G. Guzik[c], A. Insolia[h], C.N. Knott[e], S. Ko[d], C. Kuo[d],
P.J. Lindstrom[b], J. Mazotta[d], M. McMahon[c], J.W. Mitchell[a],
R. Potenza[h], J. Romanski[h], G.V. Russo[h], A. Soutoul[g], O. Testard[g],
C.E. Tull[c,1], C. Tuvé[h], C.J. Waddington[e], W.R. Webber[f], J.P. Wefel[c]

(*The TRANSPORT Collaboration*)

July 2, 1996

[a] NASA/Goddard Space Flight Center, Greenbelt, MD, USA;
[b] Lawrence Berkeley Laboratory, Berkeley, CA, USA;
[c] Louisiana State University, Baton Rouge, LA, USA;
[d] Space Sciences Laboratory, University of California, Berkeley, CA, USA;
[e] University of Minnesota, Minneapolis, MN, USA;
[f] University of New Mexico, Las Cruces, NM, USA;
[g] Service d'Astrophysique, C.E.N. Saclay, Cedex, France;
[h] Universitá di Catania, INFN, Sezione di Catania and CSFNSM, Catania, Italy.
[1] Current address: Lawrence Berkeley Laboratory, Berkeley, CA, USA.

Abstract

The Heavy Ion Spectrometer System (HISS) at the LBL Bevalac provided a unique facility for measuring projectile fragmentation cross sections important in deconvolving the Galactic Cosmic Ray (GCR) source composition. The general characteristics of the apparatus specific to this application are described and the main features of the event reconstruction and analysis used in the TRANSPORT experiment are discussed.

1 Introduction

One of the fundamental goals of Galactic Cosmic Ray (GCR) astrophysics is to relate measurements of the elemental and isotopic spectra of cosmic rays to the original composition at the galactic cosmic ray sources (GCRS). Accomplishing this goal will provide important information regarding the mechanism(s) responsible for accelerating cosmic ray nuclei to high energy, the mixture of material, possibly from exotic astrophysical sites, making up the GCRS matter, the nucleosynthesis of heavy matter at such sites, and the evolution of matter in the galaxy. Key to this task is being able to correct the measured spectra for the modifications resulting from the atomic and nuclear interactions of the GCR with the interstellar medium (ISM). Given the ability to predict the population of the different secondary fragments produced in these collisions, it is possible to determine the extent of the propagation effects by examining the ratios of pure secondary species (those with little or no GCRS components) to primary species. Currently the ability to determine the GCRS composition in many instances is limited by the accuracy of the nuclear fragmentation data and models rather than by the GCR measurements themselves. A critical next step to achieve a better understanding of the GCR source population, acceleration, and propagation is the accurate measurement of cross sections for expected primary GCR nuclei on targets of the most abundant ISM nuclei, H and He, over a broad range of energies, the focus of the TRANSPORT collaboration experimental program.

Projectile fragmentation is known to produce secondary isotopes having velocities nearly equal to the incident beam velocity [1]. Secondaries, or fragments, have transverse momentum distributions that depend on fragment and projectile mass and are typically gaussian [2] with widths of a few hundred MeV/c [3]. In peripheral collisions, the products typically consist of a large fragment having mass and charge near that of the projectile accompanied by a few low mass fragments (e.g. neutrons, and hydrogen and helium isotopes). In central collisions, there may be many low mass fragments produced. Between these two extremes lies a region of multi-fragmentation in which medium and low mass fragments are produced in the same collision. Peripheral and multi-fragmentation regimes contribute significantly to the production cross sections for fragments that range in size from the projectile (i.e., beam) mass, A_P, down to one half that mass, $A_P/2$, the range of interest in this experiment. To be sensitive to this range of fragments and still achieve iso-

topic identification, the large aperture Heavy Ion Superconducting Spectrometer (HISS) at the Lawrence Berkeley Laboratory (LBL) was chosen as the facility for the initial measurement of the TRANSPORT group.

The program conducteded at LBL included measurements of the interaction cross sections and the single particle inclusive elemental and isotope production cross sections for a variety of astrophysically important heavy ion beams from He to Ni at energies from 338 A MeV to 894 A MeV incident on a liquid hydrogen (LH_2) target. These data were collected during two separate running periods, April 1990 and April 1991.

This paper describes: (1) the general theory of the measurements (section 2), with the relevant formulae used to extract cross sections from the raw experimental data; (2) the experimental apparatus used in the TRANSPORT heavy ion fragmentation program and the detector calibration procedures (section 3); (3) an outline of the analysis procedure (section 4), which includes a description of the particle identification (PID) method based on measurements of the incident beam vectors and of the rigidity, charge, and velocity of each outgoing fragment produced in the interactions, the analysis of neutron data, and the discussion of the possible sources of error; and (4) the conclusions (section 5) about the current status and future prospects of the TRANSPORT program.

2   General Theory of the Measurement

The detailed formulation for analyzing the experimental data depends upon the configuration of the target where the interaction takes place. Many similar experiments have adopted the so-called 'thin target approximation' for its simplicity. However, a 'full' treatment is usually required when all other factors are considered. In our particular application, the analysis starts with a 'thin target approximation'. A full analysis, including target thickness and system acceptance effects, is applied to yield the final cross section values. In the following sections we present a brief description of the analysis procedure. In addition, we include a more detailed cross section analysis formulation in the Appendix A, as such treatment is not easily found in the literature.

2.1 Thin Target Measurement of Cross Section

In the case where a projectile $P \equiv F_0 \equiv (Z_P, A_P)$, incident on a thin self supporting target T, produces fragments $F_i \equiv (Z_F, A_F)$, the cross section for producing F_i ($0 < i \leq n$) is given by the well known formula (see Appendix A):

$$\sigma_T(0 \rightarrow i) = \frac{1}{t} \cdot \frac{N_i}{N_{TOT}} \tag{1}$$

where N_i is the number of fragments F_i, N_{TOT} is the number of incident projectiles and t is the thickness of the target. This is a very good approximation for a thin target where $t \ll \frac{1}{\sigma_{T,TOT,0}}$ and $\sigma_{T,TOT,0}$ is the total cross section. For a hydrogen target, the thickness t is determined by

$$t = \frac{N_A \cdot \rho \cdot L \cdot 10^{-27}}{A_H} mb^{-1} \tag{2}$$

where N_A is Avogadro's number, A_H is the atomic weight of hydrogen, ρ is the target density in g/cm^3 and L is the target geometric length in cm.

Because of the simplicity of Eq.(1), it is easy to implement the corrections for the finite size and efficiency of the detector system, as well as for the background subtraction for those targets where the container/support material is not negligible. In reality, even for such thin targets, determining N_i and N_{TOT} involves more than simple counting techniques, as they must incorporate such considerations as detector system acceptances, $\alpha_i \equiv \alpha(Z_F, A_F)$, detection efficiencies of the system, $\eta_i \equiv \eta(Z_F, A_F)$, normalizations between runs taken with different triggers, and spurious fragment production in the target supports and beam line materials.

The true produced population of the ith fragment, N_i, can be simply related to the experimentally detected population, $N_{i,det}$, by

$$N_i \equiv N_i(t) = N_{TOT} \cdot \sigma_T(0 \rightarrow i) \cdot t = \frac{N_{i,det}}{\alpha_i \cdot \eta_i \cdot R_{I:B}} \tag{3}$$

where $R_{I:B}$ is the normalization factor between runs with different triggers (see section

4.4). The true total number of incident beam particles, N_{TOT}, is also obtained experimentally as the sum over all possible fragments, including non-interacted projectiles. That is:

$$N_{TOT} = \sum_{i=0}^{i=n} N_i \qquad (4)$$

The complication introduced in the experimental determination of $\sigma_T(0 \rightarrow i)$ by the background signals from reactions in the target container and/or support and in materials along the beam line can be accounted for by repeating the measurement using an empty target vessel, $T0$, in place of the filled target, T, and substituting Eq.(1) with:

$$\sigma(0 \rightarrow i) = \frac{1}{t} \cdot \left(\frac{N_i^T}{N_{TOT}^T} - \frac{N_i^{T0}}{N_{TOT}^{T0}} \right) \qquad (5)$$

where N_i^j are given by Eq.(3) and the N_{TOT}^j by Eq.(4)

2.2 Finite Size Target

The cross section calculations for a realistic target of finite thickness and transverse diameter are more complicated. There are a number of considerations which have to be resolved before final cross sections can be evaluated.

(1). The losses of incident beam projectiles and fragments within the target via interactions with either the target or container materials cannot be ignored. The target used for this experiment (see section 3.2) contains ≈ 0.25 g/cm^2 of liquid hydrogen, and the windows of the target vessel have a total thickness of ≈ 0.16 g/cm^2. There are two major factors that significantly affect the cross section calculations. The first is the loss of beam particles through the target. This effective beam reduction, if not corrected, reduces the measured fragment relative yields. The second is the loss of background fragments, created in the front target window, through the hydrogen volume. This reduction of background is not present for the mass dummy used for target out runs ($T0$). Therefore, this makes the background, measured by $T0$ runs, higher than the true background and again, if not corrected, reduces the measured fragment yields. In addition, there are finite contributions from secondary production, i.e. fragments produced from other fragments

with higher (Z, A).

(2). The detectors and target acceptances, in general, depend upon (Z_F, A_F). If the target is not very long, as is the case in the present experiment, we can use the mean acceptance of the system, taken along the whole thickness t. However, depending on the effects of transverse momentum and scattering, the produced fragments F_i may escape the target volume prematurely, especially for long targets and low incident energies.

(3). The acceptances for various post-target detectors are also dependent upon (Z_F, A_F), and have to be evaluated individually.

The general equation for transport of projectile nuclei through a realistic target is

$$\frac{dN_i(z)}{dz} + N_i(z) \cdot b_{i,T}(z) \cdot \sigma_{T,TOT,i} = \sum_{j=0}^{j=i-1} N_j(z) \cdot b_{j,T}(z) \cdot \sigma_T(j \rightarrow i) \qquad (6)$$

where $z = N_T \cdot s$, s is the depth of the interaction point inside the target and N_T the number of target nuclei per unit area, $N_k(z)$ is the net number of fragments of the type k present after the beam has traversed a depth z inside the target, $\sigma_{T,TOT,i}$ is the total cross section for the production of secondary fragments and $b_{i,T}(z)$ is an acceptance term which reduces identically to 1 or to the Kronecker $\delta_{i,0}$ for targets with sufficiently large or sufficiently small transverse diameter, respectively. The fragments, F_i, are ordered from the projectile F_0 to the smallest possible fragment F_n, i.e. $0 \leq j \leq i \leq n$. Cross sections for pick-up of nucleons from the target are negligibly small within the energy range and projectile-target combinations for this experiment, and, consequently the corresponding terms in Eq.(6) can be ignored. A detailed derivation of Eq.(6) can be found in Appendix A.

The ith fragment population measured by a detector, $N_{i,det}$, is now bound to the true number of produced i^{th} fragments by the integral equation

$$N_{i,det} = \eta_i \cdot \int_0^t \alpha_{i,T}(z) \cdot \frac{dN_i}{dz} \cdot dz \qquad (7)$$

which, for realistically thin targets at given incident energy, as in the present case, reduces

6

to

$$N_{i,det} = \eta_i \cdot \alpha'_{i,T} \cdot N_i \qquad (8)$$

and

$$N_i(i \neq 0) = \int_0^t dN_i \qquad (9)$$

where $\alpha'_{i,T}$ is the mean acceptance of the detector system taken along the target itself.

The only methods of solving the general transport equation, Eq.(6), are numerical. In practice, the cross sections from this experiment are calculated in two steps using a combination of both Eq.(6) and Eq.(5). First the thin target approximation (i.e., Eq.(5)) is applied to obtain the thin target cross sections, with all detector acceptances corrected. Then Eq.(6) is numerically solved with the deduced thin target cross sections used as the initial values. The entire target is divided into many thin slabs so that Eq.(1) is applicable to each slab. Acceptance corrections are applied to each thin slab. Secondary interaction cross sections are estimated from the Webber et al. parametric prediction [4] and total interaction cross sections are calculated from this experiment [5]. An iterative process is used to calculate the final fragment yields for both LH_2 and mass dummy $T0$ targets runs. The cross sections $\sigma_T(0 \to i)$, which we want to measure, are varied until the calculated yields match with the experimental data. As been pointed out, the major corrections come from effective loss of beam projectile and background loss. Due to the fact that the hydrogen thickness is only ≈ 0.25 g/cm^2, the secondary production in most cases is not significant, except for channels with very large charge and mass change.

3   The Heavy Ion Spectrometer System (HISS) at LBL

The basic apparatus of the magnetic spectrometer, HISS, as it was configured for this experiment is shown in figure 1. It can be divided into three main subsystems.

1. The upstream detector system (UDS), including the target, through which the beam passes before entering the magnet.

2. A simple superconducting dipole magnet with a 3 m pole diameter, a 1 m gap, and able to generate up to 7 Tm of bending power.

3. The downstream detectors to detect and identify particles emerging from the magnet. These are: (1) a drift chamber (DC) for tracking the charged products; (2) a time-of-flight (TOF) wall; (3) a multifunctional neutron spectrometer (MUFFINS).

A general discussion of the standard set of HISS detectors for charged particles has been published [6] and information about the neutron detector followed later [7]. Here we describe only the application of these detectors to heavy ion fragmentation measurements.

The magnetic spectrometer method of particle identification is based on the premise that a given isotopic fragment, $F_i \equiv (Z_F, A_F)$, can be identified by measuring its charge, Z_F, rigidity, R_F, and the reduced velocity, β_F, giving A_F by:

$$A_F = \frac{R_F \cdot Z_F \cdot e \cdot c}{\beta_F \cdot \gamma_F \cdot m_N \cdot c^2} \tag{10}$$

where m_N is the nucleon mass. Z_F is measured both in the UDS and TOF wall, while the combination of the trajectory information from the UDS and the tracking in the DC after the magnet determines R_F, provided the field map is known. The TOF wall, together with the start scintillator in the UDS, is used to determine the time of flight, measuring β_F.

3.1   Upstream Detection System

The major functions of the Upstream Detection System (UDS) are to provide the primary event trigger, to monitor beam quality, to provide a reliable beam count, to determine the position of an incident beam particle on the liquid hydrogen (LH_2) target, to provide a post-target charge identification, and to return an upstream three vector for each fragment. The mass resolution of a magnetic spectrometer depends on accurate measurements of the trajectories of the incident particle and of the reaction products.

As shown in figure 2, the UDS consists of two position sensitive detectors (PSD1 and PSD2), three small scintillator paddles (S1, S2 and BV), a large diameter, low grammage silicon detector (SSD), three large veto scintillators having holes at their centers (1 cm diameter for V1, 2.54 cm for V2 and 4.5 cm for V4), a veto detector with an adjustable aperture (AV) and wire chambers (WC5, WC6, WC7) for beam tuning. The LH_2 target

vessel (TGT) is placed between V2 and V4. A Fiber Scintillator Hodoscope (FISH), designed to measure fragment trajectories, is placed between SSD/BV and HISS.

These detectors were mounted on a specially designed optical bench which not only provided a relative reference frame, but also aided placement reproducibility when detectors had to be removed for reconfiguration or repair during the course of the experiment. Scintillators S1 and V1 are placed at the beam focus about 10 m upstream of the target where S1 functions as the start detector for the TOF system. V1, V2 and the adjustable veto AV, are used to veto any beam particles outside the acceptable phase space of the system. These scintillators combined with S2 constitute one of the two main triggers for the experiment (the other, INT, is defined in section 3.3):

$$BEAM = S1 \cdot \overline{V1} \cdot \overline{AV} \cdot S2_L \cdot \overline{S2_H} \cdot \overline{V2} \cdot \overline{PRE} \cdot \overline{V4} \tag{11}$$

$\overline{PRE}$ (preceded) was generated by a coincidence between $S1 + V1$ and the slightly delayed output of an UpDating-One-Shot (UDOS) gate triggered by $S1 + V1$. A coincidence occurs only if the particle was preceded by another particle within the pre-set width of the UDOS. This insures that no beam particle or fragment preceded a valid trigger within a 15 - 300 ns time period. Two discriminator levels were applied to the signal from S2 to reject events with an energy deposit significantly different from that of the projectile. These S2 signals, $S2_L$ and $S2_H$, acted as a single-channel analyzer to block prefragmented beam particles or multiple beam particles (with < 20 ns separation) from triggering the system. The corresponding discriminator levels were adjusted for each beam. A scaler count of the $BEAM$ trigger was used to calculate the quantity N_{TOT} referenced in Eq.(1).

Beam quality was monitored by checking for adequate time separation between beam particles entering the system, assuring beam species purity, eliminating beam halo and restricting beam particles to the proper phase space. Checking the time separation between incoming beam particles is accomplished by bracketing every particle entering the system from $S1 + V1$ with a 2 μs gate from a second UODS (ORTEC 404A). The coincidence between this gate and a preceeding or following beam particle is put into a coincidence register to flag the event being processed as possibly contaminated. The 2 μs window was dictated by the 0.6 μs peaking time of the SSD shaping amplifier.

The purity of the beam accepted was determined by a combination of S1 and S2 detectors and a bending magnet placed upstream of S1. The pulse height of the S2 signal was used in the trigger to veto beam particles with incorrect charge, while any beam particles with an incorrect charge to mass ratio were swept into the V2 veto by a bending magnet. During runtime, the S1 counting rate and the ratios $S1/V1$, $S2/V2$ and $N_{TOT}/BEAM$, were used to monitor any significant drifts during the run.

PSD1 and PSD2 were placed at about 1 m and 2 m upstream of the liquid target to vector the incoming beam particles. Both PSD1 and PSD2 are constructed with an internal scintillating fiber grid for calibration purposes. PSD1 and PSD2 were used off-line to reject any events originating from beam particles outside acceptable phase space limits. Data from the combination of V2, PSD1, and PSD2 determined the projectile acceptance, $\alpha'_0 \equiv \alpha'(P) = 1$, as referenced in section 4.2.1

3.1.1 Upstream Vector Calibration

A crucial function of the UDS was to obtain an upstream vector for each beam particle. For this task it was necessary to produce an internal calibration of both PSD1 and PSD2 for each beam, using an internal scintillating fiber grid. At the beginning of each beam-energy change, calibration data files were taken in which the "OR" of each grid's fibers was required as a trigger condition:

$$FIBER = (S1 + V1) \cdot (Fibers_{PSD1} + Fibers_{PSD2}) \tag{12}$$

The PSD outputs corresponding to the crossing points of the fibers, as shown in figure 3, are determined and placed into lookup files where they are cross referenced with the known physical locations of the fiber crossings. These lookup files are used for interpolating the position in the PSD detectors for each beam particle within an error of $\sigma_{PSD} \approx 0.1$ mm. To protect against possible detector drifts, each data file was checked for any run dependent offsets by imaging the fibers for each file. In most cases there were no offsets. The values for PSD1 and PSD2 are then used to calculate a three vector for each beam particle and to project the beam particle's position to the LH_2 target, and further to MUFFINS.

3.2 Targets

A schematic of the liquid hydrogen (LH_2) target cryostat and control system used in this experiment is shown in figure 4. The target assembly (bottom) contains two target vessels of length 2.7 cm and 20.0 cm, respectively, and diameter 7.0 cm in a common cryostat. The vessels are stainless steel cylinders, with 100 μm titanium windows, wrapped with copper tubing to provide heat exchange with a 37 liter dewar of liquid helium mounted beneath. The entire assembly is, in turn, surrounded by multiple layers of super-insulation, a copper heat shield, and a vacuum jacket constructed from a corrugated stainless steel cylinder with machined aluminum endcaps and another set of 100 μm titanium windows. Both target vessels are equipped with 1 cm stainless steel emergency relief lines that exit through the front of the vacuum jacket. The temperature and pressure were monitored and recorded for each run.

The LH_2 target is operated at a pressure of 2 atm which causes the entrance and exit windows to bulge into the vacuum vessel. Thus, the geometric path length (in cm), L, of an incident projectile in the liquid depends on the point of impact on the face of the LH_2 target and on the trajectory relative to the symmetry axis of the target.

Due to the time required to drain and reliquify the hydrogen in the LH_2 target, a "mass dummy" target was used to emulate an empty target vessel and obtain the value of $N_{i,det}^{T0}$ referenced in Eq.(3) through Eq.(5). The "mass dummy" vessel was installed to one side of the dewar containing the actual LH_2 target, so that "target in"/"target out" changes could be performed quickly.

3.2.1 LH_2 Target Thickness

The most important parameter associated with the target is the actual thickness in g/cm^2, $\rho \cdot L$, of liquid hydrogen traversed by the beam particles. The target is designed to operate in the phase space region where the LH_2 temperature changes slowly enough that the hydrogen never strays far away from the equilibrium state. Because of the one to one relationship between the temperature and pressure at equilibrium, the density depends only slightly on the pressure of the liquid hydrogen in the target, and we derive the LH_2 density from the temperature, using the value of the pressure for minor corrections.

Figure 5 shows the target vessel temperature measured during a typical portion of the April 91 run (top) as well as the relationship between temperature and LH_2 density (bottom). The final density was determined to be in the range of $\rho = 70.6 \pm 0.9$ kg/m^3 and was found to be essentially constant during each run. The liquid temperature and pressure were very closely monitored, independently, so that any density variation could be identified and controlled to less than 0.2% during the actual data taking period. The uncertainty is dominated by systematics in the exact shape of the saturation curve relating density and temperature. The actual target thickness must be derived for each beam by knowing the density of the liquid and the pathlength distribution of the beam through the target vessel.

After initial pressure tests, the target vessel titanium windows are permanently contorted into a spherical shape with ≈ 136 mm radius of curvature. Thus the titanium windows bow out in the center by about 4.5 mm at the furthest extent on each end of the target, introducing a maximum of $\approx 33\%$ pathlength variation across the entire thin 2.7 cm target. A realistic beam has a finite extent over the curved target surface but varies in intensity over the area. With the help of upstream vectoring, the exact beam profile was determined for each run. Thus the uncertainty in the mean target thickness is actually dominated by the accuracy of the upstream vectoring, which, in turn, is dominated by the uncertainty in the survey of the physical location of the position sensing detectors, PSD1 and PSD2.

To evaluate the target thickness uncertainty, the distributions of thickness were derived for beam profiles generated by moving one of the position sensing detectors ± 2 mm, the survey uncertainty, along both the horizontal and the vertical axes. The variation of the mean target thickness was then used to derive the final target thickness, typically 0.24 g/cm^2 for the thin target, and the resulting uncertainty, $\Delta t/t$, normally less than 3%.

3.3   Interaction Detectors

The charge of the projectile fragment, Z_F is measured downstream of the LH_2 target by the combination of two detectors, BV and SSD. The BV detector consisted of a 7 cm high by 10 cm wide piece of 0.3 cm thick Bicron 408 plastic scintillator which was

viewed by two RCA 8575 photomultiplier tubes, one on each side. The SSD was a 5 cm diameter, 0.1 cm thick, lithium-drifted-silicon solid-state detector. This detector is positioned just down stream of the LH_2 in a light-tight, nitrogen filled container with 5-mil aluminum-foil windows at the entrance and exit. A DC bias of 400 V was applied to the SSD, resulting in a leakage current of less than 10nA. The SSD output was amplified using a Tennelec TC-178 pre-amplifier and a TC-244 shaping-amplifier set for triangular shaping. A peaking time of 0.6 μs was selected to optimize both charge resolution and beam rate tolerance. The amplifier gain was set to register the average beam peak at $\approx 80\%$ of full scale of the ADC. This value was chosen to encompass 99% of all incoming beam particles, to maximize the charge resolution from the detector, and to be able to flag overflow events. For the 1991 runs the SSD detector was coupled with a scintillation detector, V4, which was used to eliminate events containing fragments that impacted the edge or mounting ring of the SSD. The V4 detector consisted of a 15 cm^2, 3 mm thick piece of Bicron 408 with a 4.6 cm diameter hole positioned to be concentric with the SSD detector. A typical raw data plot of the resultant SSD signal versus that from the BV scintillator is shown in figure 6 (top) for a ^{32}S beam at 770 A MeV, and discussed in the next section.

The second principal function of the SSD detector and BV scintillator is to determine if the incoming beam particle underwent an interaction in the target. The discriminator threshold on the sum of the BV PMT outputs was set at a level between Z_P and Z_P - 1 and the signal was used in the second major trigger for the experiment which tagged those events in which a nuclear collision occurred:

$$INT = BEAM \cdot \overline{BV} \qquad\qquad (13)$$

An SSD vs. BV plot for data taken with the INT trigger is shown in figure 6 (bottom) where the rejection of uninteracted beam is evident. Note that the BV threshold setting produces an underestimation of the $Z_P - 1$ fragment, but does not affect any lower charge fragments. Runs were made with both the INT and $BEAM$ triggers to maximize the number of fragments collected for a given time period and to determine the rejection efficiencies.

3.3.1 Interaction Detector Calibration

The final post-target/pre-magnet charge assigned to an event was a combination of the independent charge measurements from the BV and the SSD detectors. The first step in obtaining a charge calibration was to remove the background caused by multiple particle pile-up effects, SSD "underflows" and secondary interactions which obscure the "charge islands" shown in figure 6. The multiple particle pile-up effects occur when two or more particles pass through the detector within a few microseconds of one another. Pile-up causes the SSD detector signal to either saturate (line at the top) due to the excessive energy deposit or to be reduced (e.g. vertical stripe at about BV ADC of 700), both due to the finite period of time that it takes the shaping-amplifier output to return to baseline. While the experiment trigger included pile-up protection as mentioned earlier, it did not provide full protection. Thus it was necessary to use the event clock scalar to tag these events in the off-line analysis. Also seen in the raw data plot are SSD "underflows" (line at the bottom of the plot) which are caused by particles missing the active region of the SSD, but hitting the larger BV detector. The V4 detector was installed in the 1991 data run and removed most of these underflow events from that data set. Finally, to the left of the diagonal formed by the valid events are particles which have suffered secondary interactions between the SSD and BV detectors.

Once the background was removed the SSD signal was histogrammed and a multiple gaussian fit was used to determine the means of the charge peaks. These means were linear in Z^2 and were fit using the least square method to provide the SSD charge calibration. The BV detector has somewhat poorer charge resolution and the charge peaks were not as easily identified. For this reason we used the SSD to select a particular element. The resulting elemental histograms in BV were then fit with a gaussian distribution to determine the mean signals, which were found to be linear with Z_F.

These calibrations were performed for each beam and energy combination as the PMT tube voltages and amplifier gains were adjusted to optimize the charge resolution for each run. The calibrations were also determined for both "target in" (LH_2) and "target out" ($T0$) on each beam, as the energy deposited in the detectors was different for the two cases. After the calibrations are applied, the fragment charge is determined from a weighted

14

average of the SSD and BV signals. The relative weights were adjusted to optimize the charge resolution. The result is $\sigma_Z < 0.2$ throughout. Typical charge histograms for both the *BEAM* (top) and *INT* (bottom) trigger data are shown in figure 7 (^{32}S at 770 A MeV), where clear charge peaks can be seen down to $Z_P/2$.

3.4 Drift Chamber (DC)

The DC was used to determine the trajectories of particles emerging from the magnetic field. The DC is composed of fifteen 200 cm tall by 300 cm wide by 10 cm thick modules. Each module consists of a sense plane which is sandwiched between two high voltage planes each consisting of three planes of wires, staggered by 2 mm and held at different negative potentials to achieve the optimum field shape for the 1 cm by 2 cm cells. The wires are oriented at 0°, +30°, and −30° from the vertical to form S, T, and U planes respectively. The plane arrangement was T-S-U-S-T-S-U-S-T-S-U-S-T-S-U. The fifteen planes comprise a single gas volume which is filled with P10 (90% Ar:10% CH_4) gas and sealed on either side by a double 0.5 mm mylar window. The overall high voltage was adjusted to maximize the DC and electronics dynamic range for each beam-energy combination.

Particle positions returned by the DC, when combined with the upstream position measurements and the magnetic field map, yield a rigidity measurement, R_F, for each particle. As shown in figure 8, the DC single plane resolution is ≈ 0.25 mm in the bending plane of the magnet, which corresponds to a rigidity resolution $\Delta R/R \approx 2 \cdot 10^{-3}$ for ^{36}Ar at 546 A MeV. A more complete description of the design principles and electronics for this detector can be found in a paper by Kobayashi et al. [8]

3.4.1 Calibration and Resolution of the DC

Several steps were involved in calibrating the data from the DC before particle trajectories downstream of the magnet could be determined. A primary step was the determination of the space-to-time function which would accurately translate the drift time (given in TDC channels) into a spatial value (in microns) for any given cell in the DC. This space-time function was essentially the same for all cells of the DC; however, it did change when the voltage supplying the shaping field was changed for the different beam

and energy combinations. Thus, it was necessary to recalibrate the space-time function for each beam-energy combination.

The space-time functions for the DC were obtained using an iterative approach. Starting with an initial guess for the space-time function, the hit positions for particles passing through a single drift cell were determined and plotted versus the TDC channel. Next the particle trajectory was fit and the track residual was plotted against the hit position. These residuals are the difference between the position of the track in a given plane as calculated from the current version of the calibrations and the position predicted in the same plane from the fitted track using all other planes associated with this track. An incorrect TDC offset would cause an uneven left to right distribution with respect to time. A non-zero average residual would be caused by incorrect offsets between the different wire planes. An incorrect shape of the space to time function would introduce a tilting and/or a waving in the residual versus hit position distribution. These parameters was adjusted until the residual yielded a flat, even distribution within the cell. The effective resolution of the space-time function was further increased by using the particle's charge as determined by the drift chamber ADC values to slew correct the drift chamber TDC values.

In addition to the space-time function, it was necessary to determine the individual wire and plane offsets. Unlike the space-time curve, the wire/plane offsets were neither beam nor energy dependent but remained constant so long as there was no physical displacement of the DC.

The next step was to refine the above calibrations using information from the TOF wall. Specifically, the trajectories determined by the DC can be projected onto the individual slats in the TOF wall. By comparing the projected spot with known dimensions for these slats, the physical relation between the detectors in the experiment were adjusted to much greater precision than the ± 0.2 cm achievable by the surveyors. Over all runs, a horizontal resolution of $\Delta X_{DC} = 350 \mu$m and a vertical resolution of $\Delta Y_{DC} = 450 \mu$m was obtained.

3.5 Time-of-Flight (TOF)

A TOF system was used in this experiment to measure the charge, Z_F, and velocity, $\beta_F c$, of the fragments, and to provide a rough position measurement to complement the trajectory information obtained by the drift chamber. The time-of-flight (TOF) system at HISS consists of a central section of thin slats and outer sections of much larger slats. The central area covers 1 m × 1 m and consists of two layers of Bicron BC408 scintillator slats, 2 cm × 140 cm × 0.7 cm in size, offset to provide a 1 cm granularity. The additional 40 cm in length acts as a light guide and provides for an asymmetrical bend at both ends to allow connection of a Hamamatsu R1398 photomultiplier tube (PMT). Each PMT is covered by a 0.020 inch thick mu-metal cylinder and the whole row of PMTs is additionally shielded by 0.25 inch soft iron plates to protect them from the stray magnetic field of the HISS dipole. On either side of this central area are two layers of larger slats, 11 on each side (6 front, 5 back) with each slat of BC408 10 cm × 252 cm × 0.7 cm. At the top and bottom of the central area are two layers of larger slats, 8 each, four in front and four behind, with each BC408 slat being 20 cm × 100 cm × 0.7 cm in size. All slats in the central section have R1398 PMTs at each end, while slats in the outer section are equipped with Amperex XP-2020 PMTs.

The PMTs use active bases having 5 Darlington current amplifier circuits on the final stages to maintain output levels in high rate applications [9]. Each base provides two anode outputs, one of which is routed via 400 foot long RG58 cable to a LeCroy 2282B ADC, and the other routed to a LeCroy 4413 discriminator, whose output is sent to a LeCroy 2229 (Mod 400) TDC via 250 feet of twisted pair ribbon cable . Discriminator thresholds were set to fire at 25 mV. The lowest charge observable varied from slat to slat and from beam to beam. The high voltage was set to maximize the available dynamic range.

The UDS and timing detectors, S1, S2 and BV used similiar active bases and were read out using Phillips 704 discriminators and LeCroy 2228A TDCs modified to provide 30 ps/count. Discriminator thresholds were set at 15 % of the beam pilse height.

3.5.1 Calibration of the TOF Detector

The TOF electronics were calibrated before and after each running period and the scintillator-PMT response was calibrated for each beam-energy combination. The TDC system calibration used a set of standard cable lengths and a pulser to check sensitivity and linearity, while each ADC was calibrated using a standard pulse to check gain. Each TDC channel had a sensitivity of 30-35 ps per count and therefore could cover a dynamic range of $\approx$ 60 ns. The typical non-linearity was a smooth, monotonic function yielding < 1% of full scale.

During the setup for the first heavy ion run in 1990, it was discovered that almost half of the TOF slats had developed a highly non-uniform position-dependent response. This was subsequently determined to result from multiple areas of local crazing about 1-2 cm in extent and separated by about 10-20 cm along the length of a scintillator slat. To correct this effect, the beam was blown up to dimensions exceeding the extent of the fragment distributions and then swept across the detector by (ramping the HISS magnetic field), resulting in hits from particles whose charge and velocity were well known. Each particle also passed through the DC so that trajectories were measured and therefore hit positions on the TOF slats could be determined. From this information a response map of relative amplitude and time as a function of hit position was constructed for each slat and used to correct the slat ADC and TDC signals in the off-line data analysis. The pulse height distribution for beam particles before and after correction from a good and a crazed slat is shown in figure 9. Similarly, the TOF distribution for beam particles after correction is shown in figure 10.

Particle velocity, $\beta_F c$, is determined using the pathlengths from target to TOF slat (L_{slat}) and from S2 to target (L_{S2}) , and timing ($T_{slat} - T_{S2}$) for the fragments from the trigger scintillators to the TOF wall:

$$\beta_F c = \frac{L_{slat}}{T_{slat} - T_{S2} - L_{S2}/\beta_P c} \tag{14}$$

which, for the beam particles, reduces to

18

$$\beta_P c = \frac{L_{slat} + L_{S2}}{T_{slat} - T_{S2}} \qquad (15)$$

where $\beta_P c$ is the speed of beam particles.

The S2 detector, the closest upstream scintillator to the target, was used, because the timing from this detector is least affected by energy loss of the beam in traversing the bulk of the UDS detectors. The energy at the target for some of the lower energy, higher charged beams varied by as much as 5% from the original kinetic energy. But when the dependence of the T_{S2} signal on beam particle velocity and position onto S2 is removed, the intrinsic resolution of the S2 detector is determined to be $\sigma_{S2} = 50$ ps.

To obtain the actual flight time, $(T_{slat} - T_{S2})$, the raw signals were corrected for ADC slewing, TDC offsets including cable delays and light propagation delays in the slats, and for the non-linear effects due to TOF wall degradation discussed above. TDC offsets are the easiest to be corrected, making use of Eq.(15) applied to the signals produced by beam particles when sweeping the beam along the TOF wall. At the end, typical timing resolutions in the neighborhood of $\sigma_T = 150$ ps were obtained. The pathlengths, L_{slat}, for the different particles were calculated from the known length of the central beam ray and the relative hit positions in the TOF wall for each fragment. The resulting pathlength, L_{slat}, was within 0.3% of the true value, making the error of the particle velocity $\sigma_\beta/\beta = \pm 0.2\%$.

3.6 MUFFINS

Neutrons emitted at near projectile rapidity in this experiment were detected with a MUltiFunctIonal Neutron Spectrometer (MUFFINS), a high efficiency neutron TOF detector. MUFFINS is a position sensitive detector made from 30 coaxial NE102A scintillator discs, 1 m diameter and 3 cm thickness, spaced 6.5 cm from each other. There are 6 PMTs equally spaced around the edge of each disc forming a regular hexagon. Each PMT uses the same active base used for the TOF wall and similarly has two identical anode outputs. One was sent to a LeCroy 4413 discriminator, which stops the LeCroy 2229 TDC, and the other to a LeCroy 2282 ADC through a small preamplifier (not used in the 1990 runs). The MUFFINS detector was placed at 0° downstream of the HISS

19

dipole at about 9 m from the LH_2 target. MUFFINS segmentation enables it to measure neutron multiplicities up to and possibly greater than N_t/N_n, that is the total number of discs, N_t, divided by the number of those which are contemporaneously excited by the same neutron, N_n.

Previously, neutron detectors have achieved the required degree of spatial resolution by using narrow scintillator bars whose height and width produced the necessary granularity. The detection efficiency and spatial resolution for the MUFFINS design is equivalent to a traditional counter composed of 2355 1cm × 3cm × 1m bars, while requiring only 4% of the associated electronics. The scintillator discs behave as scintillator slats for the determination of time and position of hits. Using multiple elliptical coordinate systems (MECS) [10], it can be shown that the time at which a particle impacts a disc can be decoupled from the position at which it strikes the disc. Both the spatial distribution for individual neutrons and a determination of their velocity, and hence energy, can be obtained by employing the MECS technique.

The two main purposes for detecting neutrons in this experiment were to make a measurement of the neutron stripping cross-section (the isotopic cross section at the beam charge) and to have some indication of the centrality of the collision through the measurement of the neutron multiplicity. For these purposes it was necessary to achieve a high neutron detection efficiency, which is given, for each disc, by the product of acceptance $\alpha(Z = 0)$ and intrinsic efficiency $\eta(Z = 0)$, that is: $\varepsilon = \alpha(Z = 0) \cdot \eta(Z = 0)$. Using N discs provides a total intrinsic neutron efficiency given by

$$\eta(Z = 0) = 1 - e^{-N \cdot \eta_d} \tag{16}$$

where η_d is the intrinsic neutron detection efficiency of a single disc. Given that $\eta_d \approx 3\%$ for our beam energies, then $\eta(Z = 0) \approx 60\%$, ensuring a measurement of the total neutron stripping cross section with reasonable error within the allotted beam time.

The beam and other particles of charge $Z_F > 2$ could not reach the MUFFINS detector when the magnetic field was on. However, charged pions and protons emitted from the target at sufficiently large angles with respect to the beam did reach MUFFINS

even when the magnetic field was on. For this reason, the first disc was typically put in anti-coincidence when analyzing the data. To assure no charged particles traversed the detector, hits were accepted only from events in which the first disc did not give any signal.

During the 1990 runs, a small prototype of MUFFINS (3 discs, each incorporating only 5 PMT's) was used. Hence it was not possible to measure either the stripping cross section nor the neutron multiplicity with any accuracy. However, spectra and angular distributions of neutrons were obtained for that dataset.

3.6.1 MUFFINS Calibrations

Beam particles were transported directly to MUFFINS by turning the HISS dipole off at the beginning of each run with a new beam ion or energy. In these runs, MUFFINS' discs acted as TOF walls for beam particles, so that β_P was calculated using pathlength and timing with an equation similar to Eq.(15). Knowing $< \beta_P >$, it was possible to determine the TDC offsets for each PMT channel, after correction for slew effects using the ADC data.

Although the geometrical efficiency for light collection was low, it was necessary to use in-line 10X attenuators for beams of ^{32}S and heavier and this attenuation were taken into account when computing the slewing corrections. By applying the MECS method [10] discussed above to this TDC corrected data, we were able to obtain the beam profile shown in figure 11 for ^{40}Ca at 565 A MeV. The MUFFINS detectors had timing resolution of $\sigma \approx 60$ ps, which remained constant for all ion and energy combinations studied, even though the beam profiles differed. This timing resolution is in good agreement with the results of simulations, allowing us to derive a timing resolution for neutrons of about 120 ps.

In 1991, a beam of 794.5 A MeV ^{4}He was used at the beginning of the experiment. MUFFINS data with ^{4}He were taken by triggering on two small (25 mm × 25 mm × 1.5 mm) SLF and SLB scintillators, both placed along MUFFINS central axis, one upstream and one downstream of the spectrometer, respectively. This data, taken using the calibration trigger,

served as the definitive time calibration for the MUFFINS system. TDC offsets were obtained after correction for slewing effects using the ADC data from each PMT. For each beam used in the experiment, the calibration was re-checked by turning off the HISS magnetic field at the beginning of each set of runs and allowing beam particles to directly impact MUFFINS.

3.7 Data Acquisition System

The TRANSPORT experiment used the VME-based multi-processor data acquisition system described by McParland et al. [11]. This system consisted of a set of microprocessors installed on a common VME back plane. Each processor was capable of acquiring data directly from one or more CAMAC crates via a CAMAC interface module using the VMX bus. The resulting data from each event were formatted and constructed in a single large memory array. The accumulated data were then queued to a data logging or communication process which transmitted them via Ethernet to a central VAX facility for disk storage and taping. The data disk was mounted cluster wide, hence once the data was stored, it was accessible by other workstations on the cluster. These workstations were used for various diagnostic programs as well as performing the data analysis tasks to be discussed later.

The acquisition system was controlled by programs executed in the host VAX. VME-diag, one of the primary control programs, provided an on-line display of the state of each of the major components of the data acquisition system. Further, each CAMAC interface was capable of being accessed by this program, thereby making it possible to test the various CAMAC modules using programs executing on the host VAX.

4 Analysis

4.1 Methodology

A flow chart of the analysis scheme for the experiment is shown in figure 12. In the first phase of the analysis, the data regions pertinent to each detector subsystem are

extracted and the detector calibrations discussed above are applied to extract a detector-oriented data subset. At this stage, the analysis bifurcates into an upstream branch and a downstream branch, which proceed in an independent fashion. This methodology was employed to enable reporting of total charge changing [5] and elemental [12] cross sections in a timely fashion without impeding progress toward the ultimate goal of isotopic cross sections. All major components in the upstream analysis ("good" beam characterization, BV/SSD charge calibrations, beam vector calibrations, target thickness calculations, target density and the upstream fragment acceptance) are completed prior to the level 2 processing where the upstream and downstream analysis are merged to enable isotopic and differential cross section measurements.

While the analysis of the upstream detectors is proceeding, those parts of the data associated with the post-magnet detectors, DC and TOF, are being analyzed to produce particle trajectories (X_F, Y_F, θ_F, ϕ_F), charge (Z_F), and flight time (TOF). The DC tracking code which provides trajectories is also used to project to the plane of the TOF wall and determine which slats were hit by which particles. It is the vertical component of this projection that is used to correct TOF slat response for the position dependence. Further, this trajectory information imposes a one to one association between particle trajectories from DC, specific charge and TOF. This, in turn, allows the determination of the fragment's flight path length and the completion of the determination of β_F (see section 4.2.2). The main problems during this procedure concern: (1) the determination of the acceptances $\alpha'(Z_F, A_F, z)$ and intrinsic efficiencies $\eta(Z_F, A_F)$ of the system for the different fragments; (2) the normalization of data taken with BEAM trigger to the data collected with INT trigger and (3) the measurement of rigidity. These problems are common to all of the types of cross sections to be extracted from this data and are discussed in the following sections.

4.2 Analysis for Charged Fragments.

4.2.1 Acceptances $\alpha'(Z_F, A_F)$ and Intrinsic Efficiencies $\eta(Z_F, A_F)$.

A simple Monte Carlo technique was developed to calculate the acceptance correction, $\alpha'(Z_F, A_F)$, for the spectrometer. The α's are also beam species and interaction depth (inside the hydrogen target) dependent. This Monte Carlo used real beam profiles measured

23

in the experiment, combined with the Goldhaber formulation [13] , and assumed persistence of velocity of the fragments. The resultant opening angle for fragments is typically a few mrads. The depth-dependence of the acceptances was integrated by dividing the target into thin slices along the z-axis (beam direction) and then using the Monte Carlo events to determine the proportion of fragments of each species from a given projectile that fall outside of the physical detectors. These calculations were checked for several systems with independent calculations using GEANT[14] and a second custom-written Monte Carlo code.

The acceptances, α's, were found to vary between 70% to 100% over all projectile and fragment systems for fragments measured in the experiment. For charge-changing cross sections, the A_F dependence of α's was removed by an using average over the same Z_F, weighted by the isotopic production cross sections calculated using parametric predictions[4].

As shown in figure 13, the main aperture restriction in this experiment was found to be the $SSD \cdot \overline{V4}$ combination; neither the TOF wall nor the DC significantly impacted the acceptance, so that $N_{det}(Z, A) = N_{SSD}(Z) \cdot Y(A)$, with $Y(A)$ the yield of isotopes of charge Z having mass A.

The beam acceptance was effectively 100% since the V2 aperture is significantly smaller than the V4 aperture. The only widening of the beam arose from the multiple Coulomb scattering in the material (target, window, and air) between V2 and V4. Thus, for beam particles, N_{TOT}, the only supplemental efficiency corrections $\eta(Z, A)$ were the result of misidentifications in SSD/BV. Since this is a random process and independent of the charge and mass of the fragments, a constant efficiency correction for the SSD, $\eta_{SSD} \approx 99.5 \pm 0.5\%$, could be employed for all runs, i.e.

$$N_{TOT} = N_{BEAM} \tag{18}$$

where N_{BEAM} is the number of $BEAM$ trigger signals counted by the scaler.

For fragments other than the beam, while acceptances depend on charge and impact

position, efficiencies are constant and equal to $\eta_{SSD} \approx 1$, with negligible errors, with the exception of the neutrons, discussed in section 4.3.

4.2.2 Rigidity Measurements and Isotope Identification

In computing the elemental cross section $\sigma(Z)$, the charge Z_F is obtained using the BV and SSD detectors. Identifying isotopic fragments include, in principle, the following steps:

(1). Demanding consistency with the charge returned by the TOF wall to assure that the fragment suffered no further interactions in transiting the system.

(2). Requiring that an associated track in the DC exists for each of the charges returned by that SSD TOF-wall restriction.

These associated tracks must trace out a proper trajectory from the interaction point in the target, as determined by the upstream vectoring detectors, to the impacted slat in the TOF wall. The fragment rigidity is then measured by determining the fragment trajectory as it curves through the HISS dipole field. This requires multiple position measurements along the trajectory to obtain vectors both into and out of the magnetic region, which are then used in an iterative procedure that begins with an initial guess of the particle's rigidity.

However, this long procedure, which is necessary for heavier beams such as Cr or Ni, can be avoided for lighter beams. An alternate method is based upon the first-order relationship between rigidity and the bending angle. We can form a rigidity-like variable R_{pseudo} (henceforth, "pseudo" rigidity) by

$$R_{pseudo} \propto X + K_{Z_F} \cdot \Theta_X \qquad (19)$$

where X is the fragment position in the bending plane of the HISS magnet (the horizontal plane) with respect to one of the edges of the DC, taken at the point where the track passes through one of the 15 planes of the DC itself, Θ_X is the angle that the downstream vector makes with the upstream one, and K_{Z_F} is obtained by taking a sample of each element, Z_F, and fitting a line through one of the isotope clumps that appear in a plot of X versus Θ_X for this elemental sample (Figure 14, top). The absolute units of R_F are

obtained by measuring the "pseudo" rigidity of non-interacted beam particles, for which the rigidity is known.

The measurement of "pseudo" rigidity of the fragments and its use in Eq.(10) give sufficient mass resolution for lighter beams, due to the high resolution of the fragment trajectory from the DC and the long flight path to the TOF wall. This is clearly shown, in the case of ^{22}Ne at 581 A MeV, from the center and bottom parts of figure 14. The corresponding mass histograms are shown in figure 15. The mass resolution is $\Delta A/A \approx 1\%$, with $\Delta A \approx 0.2amu$, and the mass peaks are clearly visible down to boron ($Z_B = Z_{Ne}/2$).

However, for heavier beams or for obtaining the fragment momentum distributions (and hence the differential cross sections useful in studying the details of the nuclear interaction process), it is necessary to use the more accurate fragment rigidity determined by tracing the fragment trajectory through the HISS field.

Once the mass has been determined, the isotopic identity of the fragments is established and their populations are extracted by fitting multiple gaussians to each element histogram (Figure 15). Since the acceptances $\alpha'(Z)$ and the efficiency η_{SSD} are both independent of A, the isotopic yields, $Y(A)$, as referred to in section 3.2.1, are easily obtained as:

$$Y_{Z_F}(A) = N_{det}(Z_F, A)/\sum_A N_{det}(Z_F, A) \qquad (20)$$

4.3 Analysis for Neutrons

Data taken in the calibration runs of MUFFINS (see section 3.6.1) were also used in calibrating the intrinsic neutron detection efficiencies of each disc as a function of position. The efficiency calibration incorporated a semi-empirical procedure involving GEANT predictions. The intrinsic efficiency $\eta(Z = 0)$ was determined by comparing simulated output pulses, produced with GEANT for charged particles passing through MUFFINS, to the corresponding outputs observed experimentally for the various PMTs using ^{4}He or other beams. This allows scale factors to be obtained, that, applied to the simulated pulses produced for neutron interactions, gives the realistic distribution of pulse heights that

one can expect in the experiment. The good events are then determined as those for which pulses overcome thresholds in the PMTs of a given disc (for the sake of simplicity we imposed, in the analysis as well as in the simulation, that all PMTs connected to a disc fired when a hit occurred in that disc). Efficiency for the given single disc, though not yet corrected for anticoincidence of the first disc with respect to the others, is then defined in the standard way, that is: $\eta\prime_d = (good\ events)/(all\ incident\ neutrons)$.

With this method, it is possible to vary the energy of incident neutrons and the position of incidence at the disc and thereby obtain the function $\eta_d(E_n, x, y)$ which is essential for the computation of total and partial cross sections of neutron production, one of which is the stripping cross section for production of beam isotopes. The uncorrected intrinsic efficiency of each disc, as obtained by this method, was typically 3.2% for neutrons with $300\ MeV < E_n < 1000\ MeV$.

The corrected η_d can also be obtained from $\eta\prime_d$ through complete simulations of the fragmentation process, but it seemed better to obtain it directly from comparison of experimental data analyzed with and without off-line anticoincidence with the first disc, as described in section 3.6. From this it was possible to estimate a reduction of efficiency of about 10% of $\eta\prime_d$, so that $\eta_d \approx 3\%$ as stated above.

The acceptance of MUFFINS discs, α_d, is simply connected to the solid angle $\Delta\Omega_d$ subtended by each disc, which in turn depends upon the disc to target distance. So, only for the smallest α_l, that of the last disc, corresponding to $\Delta\Omega_l$, is it possible to use the total intrinsic efficiency given in Eq.(16). For all the other discs there will be a small peripheral circular region for which the acceptance is slightly higher, but the intrinsic efficiency corresponds to $i < N$ discs. Due to the fact that the total length of MUFFINS is 1.8 m, the variation of solid angle with respect to the central disc was $\Delta\Omega/\Omega_C = 18\%$. It was decided to use only the particles detected inside the $\Delta\Omega_l$, for which $\alpha(Z = 0) = \alpha_l$.

4.4   Run Normalizations

Knowledge of N_{TOT} for each run is essential in order to normalize the results of different runs among them. Data in fact were taken under different conditions, depending on

the run; e.g. LH_2 or "dummy" target and $BEAM$ or INT trigger. Thus it was necessary to normalize run populations before using them in the cross section formulae. Normalizations among $BEAM$ trigger runs, independent of the target, is straightforward, since scaler counts are used. The same is true in normalizing INT trigger runs for the same target.

Normalizing $BEAM$ trigger runs to INT trigger runs for the same target is a bit more difficult. Here the $\overline{BUSY}$ veto increases the dead time in the case of the $BEAM$ trigger runs. The registration of events on tape was controlled by the computer through the $\overline{BUSY}$ veto, which is generated by a flip-flop set by the event trigger and cleared by the computer that no event can be accepted before the acquisition of the previous one has been completed. The dead time due to event acquisition is typically several microseconds per event. Due to the different rates and to the different word lengths for events generated under $BEAM$ or INT triggers, the dead times between the two triggers can be very different. Therefore, to correct for this effect, we must count all of the fragments detected by the SSD, $N(Z_F, A_F) = N_{SSD}(Z_F)$ for $Z_P/2 \leq Z_F \leq Z_P - 2$ (runs which used the INT trigger were inefficient in calibrating Z_P and $Z_P - 1$) and compare the resulting total numbers, obtaining the normalization coefficient $R_{I:B}$ by:

$$R_{I:B} = \sum_{Z_P/2}^{Z_P-2} N_{INT}(Z) / \sum_{Z_P/2}^{Z_P-2} N_{BEAM}(Z) \qquad (21)$$

This changes the value of N_{TOT}, given by Eq.(18), to

$$N_{TOT} \equiv N_{TOT,INT} = N_{TOT,BEAM} \cdot R_{I:B} \qquad (22)$$

This results into an overall systematic uncertainty in the cross sections

$$\Delta R_{I:B} / R_{I:B} = \min[(1 - R_{I:B}), \Delta\Sigma/\Sigma] \qquad (23)$$

where $R_{I:B}$ can well be very close to 1, if the dead time is about the same for $BEAM$ and INT trigger data, and

$$\Delta\Sigma/\Sigma = \sqrt{1/\sum_{Z_P/2}^{Z_P-2} N_{INT}(Z) + 1/\sum_{Z_P/2}^{Z_P-2} N_{BEAM}(Z)} \qquad (24)$$

A slightly different method is used in extracting the neutron stripping cross sections. The data taken with the interaction trigger cannot be used for this measurement since this trigger excludes both the beam and all isotopes of the beam. Using data taken with the beam trigger, the neutron multiplicities can be extracted on an event-by-event basis using information from the MUFFINS detector. The events in coincidence with the charge of the beam, measured by the SSD, give the yields of the isotopes of the beam, while those in coincidence with different charges supply an internal calibration of ε for MUFFINS, to compare with the computed value discussed in section 3.6.

4.5 Error Analysis

The error calculations are somewhat complex, and depend, of course, on the type of cross section to be measured. However, the main sources of error include statistics and fitting, effective target thickness, acceptance and efficiency calculations, normalization of INT trigger data, and thick target corrections. In practice, we first evaluate the associated uncertainties that contribute to the 'thin target approximation', Eq.(1), taking into account that $\Delta N_i^j / N_i^j \approx 1/\sqrt{N_i^j}$ ($j \equiv LH_2, T0$), by

$$\Delta\sigma \approx \sqrt{(\frac{\Delta t}{t} \cdot \sigma)^2 + (\frac{\Delta N_i^{LH_2}}{N_{TOT}^{LH_2}} \cdot \Sigma_{LH_2})^2 + (\frac{\Delta N_i^{T0}}{N_{TOT}^{T0}} \cdot \Sigma_{T0})^2} \qquad (25)$$

where $\Sigma_j = \frac{1}{t} \cdot \sqrt{(1 + \frac{N_i^j}{N_{TOT}^j})}$.

Determining N_i^j demands computation of acceptances and efficiencies, as well as fitting various peaks in the experimental data and normalizing INT trigger data, so that the ΔN_i^j contain not only the statistical error, but also the errors made in all the computations, while the N_{TOT}^j contain essentially the error of INT trigger normalization (see Eq.(21)), while the other sources of error tend to compensate one another, due to the large number of terms in the sum over N_i^j appearing in Eq.(4).

¿From Eq.(3) we have

$$\Delta N_i^j / N_i^j \approx \sqrt{\frac{1}{N_{i,det}} + (\frac{\Delta \alpha_i}{\alpha_i})^2 + (\frac{\Delta \eta_i}{\eta_i})^2 + (\frac{\Delta R_{I:B}}{R_{I:B}})^2 + \sigma_{fit}^2} \qquad (26)$$

where σ_{fit} is the relative error introduced by gaussian fitting of particle spectra to extract $N_{i,det}$. Furthermore, Eq.(22) yields

$$\Delta N_{TOT}^j / N_{TOT}^j \approx \sqrt{\frac{1}{N_{TOT}} + (\frac{\Delta R_{I:B}}{R_{I:B}})^2} \qquad (27)$$

where $R_{I:B}$ is taken from Eq.(21).

Types of uncertainties include:

• the overall survey resolution, which of ±2 mm giving typically a 2-3 mrad resolution for vectoring (5 mm error of particle on target);

• the effective target thickness error with vectoring resolution folded in, which is ≈ 3%;

• the gaussian fitting procedure, whose uncertainty depends upon the individual case;

• the normalization error, described in section 4.4, which is ≤ 1%.

For the thick target correction, the main source of uncertainty is the estimation of various secondary cross sections from the parametric formulae[4]. The uncertainties are evaluated using a Monte Carlo technique. This is done by randomly varying the secondary cross sections and repeating the calculations for the thick target (see section 2.2). The technique assumes a 10 % error in the secondary total cross sections and a 50 % uncertainty for the secondary cross sections. These numbers are chosen to overestimate, rather than underestimate, the final uncertainties. The calculations are repeated one hundred times with different sets of secondary cross sections, and the RMS deviation of the final correction for thick target was taken as the uncertainty. These thick target uncertainties are then added in quadrature with the original thin target uncertainties to form the final uncertainties.

5 Conclusions

We have described the experimental apparatus and outlined the method used to determine the fragmentation cross sections for nuclei from He to Ni in a hydrogen target at energies from a few hundred to a few thousand MeV/nucleon. With this apparatus we have been able to achieve a fragment charge resolution of 0.3 %, velocity resolution of 0.2 %, rigidity resolution of 0.2 % and a resulting mass resolution of 1 %, which corresponds to an absolute mass resolution of 0.2 amu for ^{22}Ne.

The experiment has data for over 20 beams interacting with a LH_2 target. The results for some of these projectiles have been reported [12, 15]; meanwhile analysis of the remaining datasets is underway. We expect to use this data to investigate nuclear systematics, study methods for improving single particle inclusive production cross section predictions, and directly apply our results to addressing particular problems in cosmic ray astrophysics. The ability to make reliable predictions of nuclear cross sections will only be realized by increasing the current database of known cross sections, and, with the recent demise of the LBL Bevalac, experiments such as the one described here will need to make use of heavy ion accelerators world wide, if this important work is to continue.

A APPENDIX: Thick Target Measurement of Cross Sections

A full thick target cross section formulation is the basis for all experimental cross sections calculations. Various special cases can be derived from the general formulae to be adapted to individual experimental setups. For example, the widely used thin target approximation is a case where the simplest cross section formulations (Eq. (1)) can be used. However, the general treatment is difficult to find in the literature. Therefore, we present an outline of such a treatment. The formulation includes not only the general projectile transport through the target, but also the geometric confinement of a realistic target volume.

A.1 Thick Target with Large Transverse Dimensions

Assuming that all fragments $F_i \equiv (Z_F, A_F), 1 \leq i \leq n$ where n is the smallest fragment type, produced from a projectile $F_0 \equiv (Z_P, A_P)$ incident on a target T, pass through the whole target (i.e. do not leave the sides), the number $dN_i \equiv dN(Z_F, A_F)$ of fragments of the type F_i, produced at a given point inside the target, is given by

$$\frac{dN_i}{dz} = \sum_{j=0}^{j=i-1} N_j(z) \cdot \sigma_T(j \to i) - N_i(z) \cdot \sum_{l=i+1}^{l=n} \sigma_T(i \to l) \tag{28}$$

that is

$$\frac{dN_i}{dz} + N_i(z) \cdot \sigma_{T,TOT,i} = \sum_{j=0}^{j=i-1} N_j(z) \cdot \sigma_T(j \to i) \tag{29}$$

The thickness t is determined by

$$t = \frac{N_A \cdot \rho \cdot L \cdot 10^{-27}}{A_T} mb^{-1} \tag{30}$$

where N_A is Avogadro's number, A_T is the atomic weight of the target, ρ its density in g/cm^3, and L is the target geometric depth in cm.

The simplest of equations (29) is $i = 0$ which gives the evolution of the beam projectiles inside the target: $\frac{dN_0}{dz} + N_0(z) \cdot \sigma_{T,TOT,0} = 0$. The solution is

$$N_0(z) = N_{TOT} \cdot e^{-z \cdot \sigma_{T,TOT,0}} \tag{31}$$

33

where $N_{TOT} = N_0(0)$ is the total number of incident projectiles.

For all the other values of i in Eqs.(29), we observe that the equations are analogous to those of the decay of a radioactive chain. They can be exactly solved, one after the other in order of increasing i. The solution, however, becomes more and more complicated as i increases, so that it is only practical to solve Eqs.(29) numerically. To give some idea of the solutions we notice that:

(1) The leading term in the right hand side of Eqs. (29) always contains $N_0(z)$, given by Eq.(31). Therefore, for thin targets ($t = N_T \cdot L < 0.02/\sigma_{T,TOT,0}$, where L is the total length of the target and N_T is the number of target atoms per cm^2), all the other terms can be ignored because $N_i(z) \propto z$ for $i \neq 0$.

(2) The secondary source term, $\sum N_j(z) \cdot \sigma_T(j \to i)$, increases continuously from $i = 1$ (for which it is 0) to $i = n$, while the corresponding sink term $N_i(z) \cdot \sigma_{T,TOT,i}$ behaves in the opposite way, approaching 0 for $i \to n$.

(3) For an extremely thick target $t \gg \frac{1}{<\sigma(i \to l)>}$, $N_i = 0$ for $i \neq n$, while $N_n = N_{TOT}$ (this is the main physical characteristic of a target with large transverse dimensions).

Therefore, taking into account that

$$\frac{N_1(z)}{N_{TOT}} = \sigma(0 \to 1) \cdot \frac{e^{-z \cdot \sigma_{T,TOT,i}} - e^{-z \cdot \sigma_{T,TOT,0}}}{\sigma_{T,TOT,0} - \sigma_{T,TOT,i}} \tag{32}$$

and

$$\frac{N_n(z)}{N_{TOT}} \to \sigma_{T,TOT,0} \cdot \frac{1 - e^{-z \cdot \sigma_{T,TOT,0}}}{\sigma_{T,TOT,0}} (z \to \infty) \tag{33}$$

we can write, for $i \neq 0$:

$$\frac{N_i(z)}{N_{TOT}} \approx a_i(z) \cdot \sigma_T(0 \to i) \cdot \frac{e^{-z \cdot b_i(z) \cdot \sigma_{T,TOT,i}} - e^{-z \cdot \sigma_{T,TOT,0}}}{\sigma_{T,TOT,0} - b_i(z) \cdot \sigma_{T,TOT,i}} \tag{34}$$

where $a_i(z) = 1$ for $z < 0.02/\sigma_{T,TOT,0}$, $a_1(z) \equiv 1$ and $a_i(z) \to \frac{\sigma_{T,TOT,0}}{\sigma(0 \to n)}$ as far as $z \to \infty$ and $i \to n$; $b_1(z) \equiv 1$ and $b_i(z) \to 0$ for z and i sufficiently large so that sink and secondary source terms compensate each other. t, i and $a_i(t)$ are, of course, related among

themselves. As a special case, Eq.(34) reduces to Eq.(1) for a thin target.

A.2 Thick Target with Small Transverse Dimensions (Wirelike Target)

It is worthwhile noting, from Eq.(34), that the net number of type F_i fragments is given by a difference of two exponentials, as it must be if fragments are produced from larger ones which are reduced to smaller ones by collisions with target nuclei. However, this result is valid only if the fragments produced by the projectile *do not* exit from the sides of the target. In any realistic experimental setup, this property is well approximated only for the beam itself, because it is well collimated. It may not be true for the produced fragments, which are emitted at finite angles from the beam itself. In particular, if the target were very long, this condition (and then Eq.(33)) would be satisfied only for very wide targets.

In general, scattering inside the target causes the projectile and the fragments to deviate from the original beam trajectories. Depending upon the size, both transverse diameter and longitudinal depth, particles can escape from the sides of the target. An extreme case is represented by a wirelike target, where all particles emitted at angles different from $\approx 0°$ escape. In this case, which is most likely at low energies where the angles of emission of fragments can be large, Eq.(29) becomes:

$$\frac{dN_i}{dz} + N_i(z) \cdot \sigma_{T,TOT,i} \cdot \delta_{i,0} = \sum_{j=0}^{j=i-1} N_j(z) \cdot \sigma_T(j \to i) \tag{35}$$

where $\delta_{i,0}$ is the Kronecker symbol.

Eq.(35) gives the same result for beam particles as Eq.(31), while for all the other fragments Eq.(34) is replaced by

$$\frac{N_i(z)}{N_{TOT}} \approx \sigma_T(0 \to i) \cdot \frac{1 - e^{-z \cdot \sigma_{T,TOT,0}}}{\sigma_{T,TOT,0}} \tag{36}$$

which, for a thin target, reduces again to Eq.(1).

35

Eq.(36) shows the main physical characteristic of the wirelike target: eventually, for a very thick target, all the produced fragments survive (because they escape from the target before they can interact again), contrary to the case previously discussed. The quantity of a given fragment is proportional to the cross section for its formation and their sum is equal to N_{TOT}.

A.3 Formulation for a Finite Size Target

The cross sections calculations for a realistic target with finite thickness and transverse diameter are more complicated:

- the losses of incident beam projectiles and fragments within the target via interactions with either the target elements or container materials cannot be ignored;

- system acceptances can depend on Z, A;

- depending on the angle of emission, the produced fragments F_i can escape the target volume from the side.

A more realistic equation for N_i is then given by a combination of Eq.(29) and Eq.(35), like:

$$\frac{dN_i}{dz} + N_i(z) \cdot b_{i,T}(z) \cdot \sigma_{T,TOT,i} = \sum_{j=0}^{j=i-1} N_j(z) \cdot b_{j,T}(z) \cdot \sigma_T(j \rightarrow i) \qquad (37)$$

where $b_{i,T}(z)$ is an acceptance term which reduces identically to 1 or to $\delta_{i,0}$ for targets with either sufficiently large or small transverse diameter, respectively. $N_{i,det}$ is related to the true number of produced i^{th} fragments by the integral equation

$$N_{i,det} = \eta_i \cdot \int_0^t \alpha_{i,T}(z) \cdot \frac{dN_i}{dz} \cdot dz \qquad (38)$$

which, for moderate length targets can be reduced into

$$N_{i,det} = \eta_i \cdot \alpha'_{i,T} \cdot N_i \qquad (39)$$

where

$$N_i(i \neq 0) = \int_0^t dN_i \qquad (40)$$

and $\alpha'_{i,T}$ the mean acceptances of the detector system taken along the target itself.

References

[1] D.L. Olson et al., Phys. Rev. C28 (1983) 1602.

[2] D.E. Greiner et al., Phys. Rev. Lett. 35 (1975) 152.

[3] F.P. Brady et al., Phys. Rev. C50 (1994) R525.

[4] W.R. Webber et al., Phys. Rev. C41 (1990) 566.

[5] C.X. Chen et al., Proc. 22nd Int. Cosmic Ray Conf. (Dublin, Ireland), 2 (1991) 296.

[6] J. Engelage et al., Nucl. Instr. and Meth. A277 (1989) 431.

[7] S. Albergo et al., Proc. 22nd Int. Cosmic Ray Conf. (Dublin, Ireland), 3 (1991) 784.

[8] T. Kobayashi et al, Nucl. Instr. and Meth. A254 (1987) 281.

[9] C.R. Kerns, IEEE trans. NS24 (1977), 353.

[10] S. Albergo et al., Nucl. Instr. and Meth. A311 (1992) 280.

[11] C. McParland et al, IEEE Trans. NS34 (1987) 751,1012.

[12] C.N. Knott et al., Proc. 22nd Int. Cosmic Ray Conf. (Dublin, Ireland), 2 (1991) 292.

[13] A.S. Goldhaber, Phys. Lett. 53B (1974) 306.

[14] F.G. deBilio et al., GEANT User's Guide, CERN DD/EE/84-1 (1987) 1.

[15] C.E. Tull et al., Proc. 22nd Int. Cosmic Ray Conf. (Dublin, Ireland), 2 (1991) 300.

Figure captions

Figure 1: The basic apparatus of the HISS system as it was configured for this experiment.

Figure 2: Schematic of Upstream Detection System (UDS).

Figure 3: Position maps for the PSD fibers before (top) and after (bottom) calibration.

Figure 4: Schematic of the LH_2 target cryostat and control system (top) and LH_2 target vessels (bottom).

Figure 5: Target temperature variations during a typical run period, with corresponding beams and energies indicated (top), and the entire operating region of density vs. temperature for hydrogen (bottom).

Figure 6: Plots of the raw SSD ADC vs. BV ADC for ^{32}S at 770 A MeV for BEAM trigger (top) and INT trigger (bottom).

Figure 7: Upstream charge histograms derived from the plots given in figure 6 for BEAM trigger (top) and INT trigger (bottom).

Figure 8: The drift chamber single plane resolution for ^{36}Ar at 546 A MeV.

Figure 9: The pulse height distribution for beam particles and fragments before and after correction from a good (bottom) and a crazed (top) slat of the TOF wall.

Figure 10:The TOF distribution for beam particles after correction.

Figure 11:Beam spot and profile as returned by MUFFINS for 565 A MeV ^{40}Ca, along with typical position and time resolutions achieved.
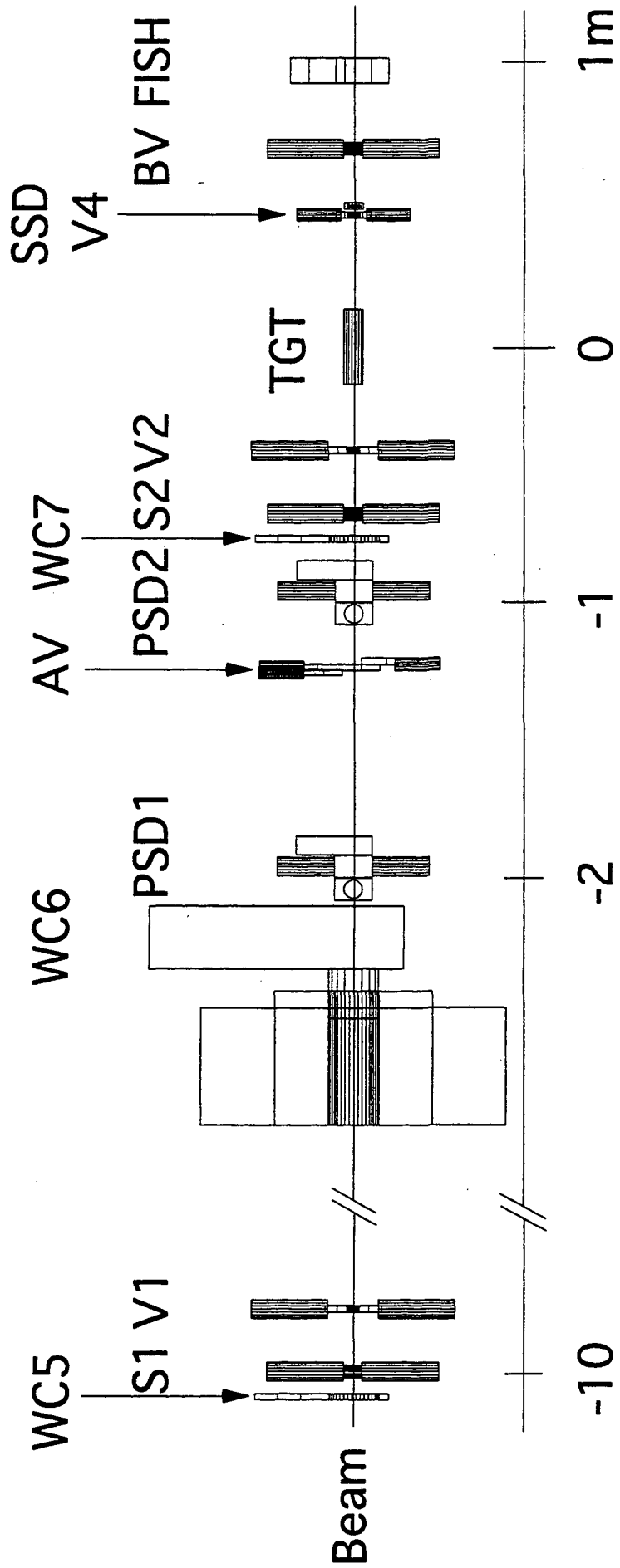
Figure 12:Flow chart of the HISS data analysis.

Figure 13:Acceptance of downstream detectors and SSD as a function of rigidity and transverse rigidity.
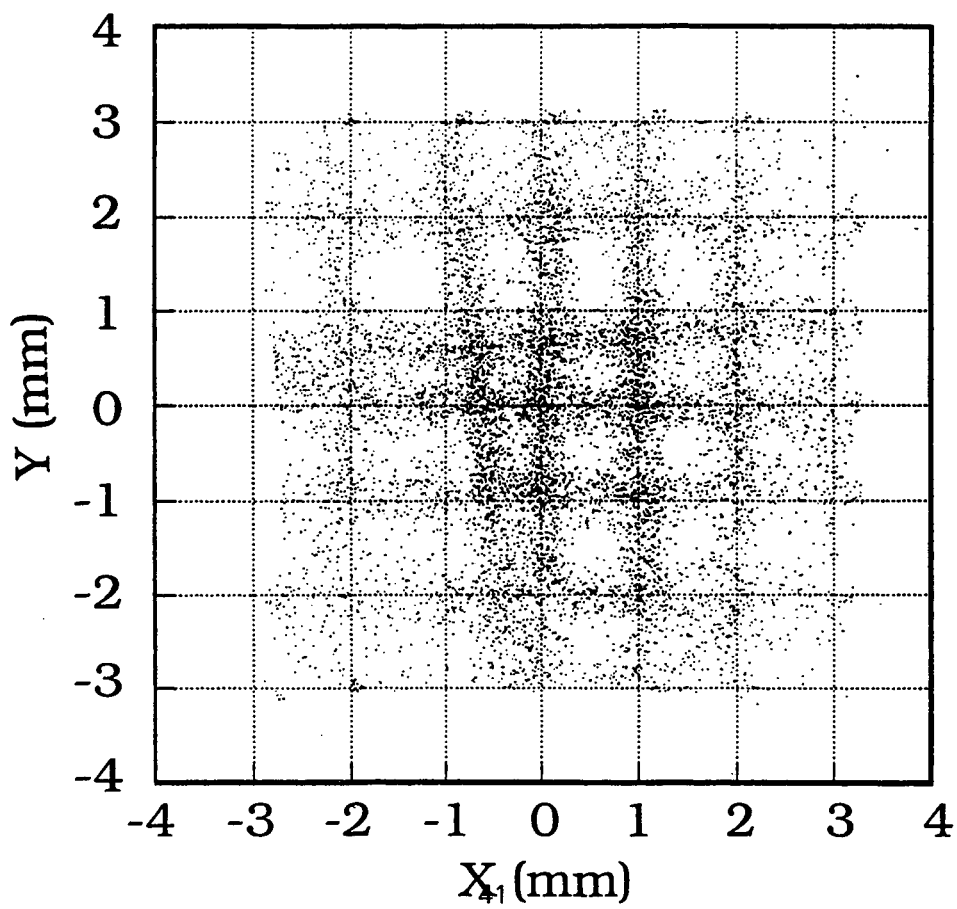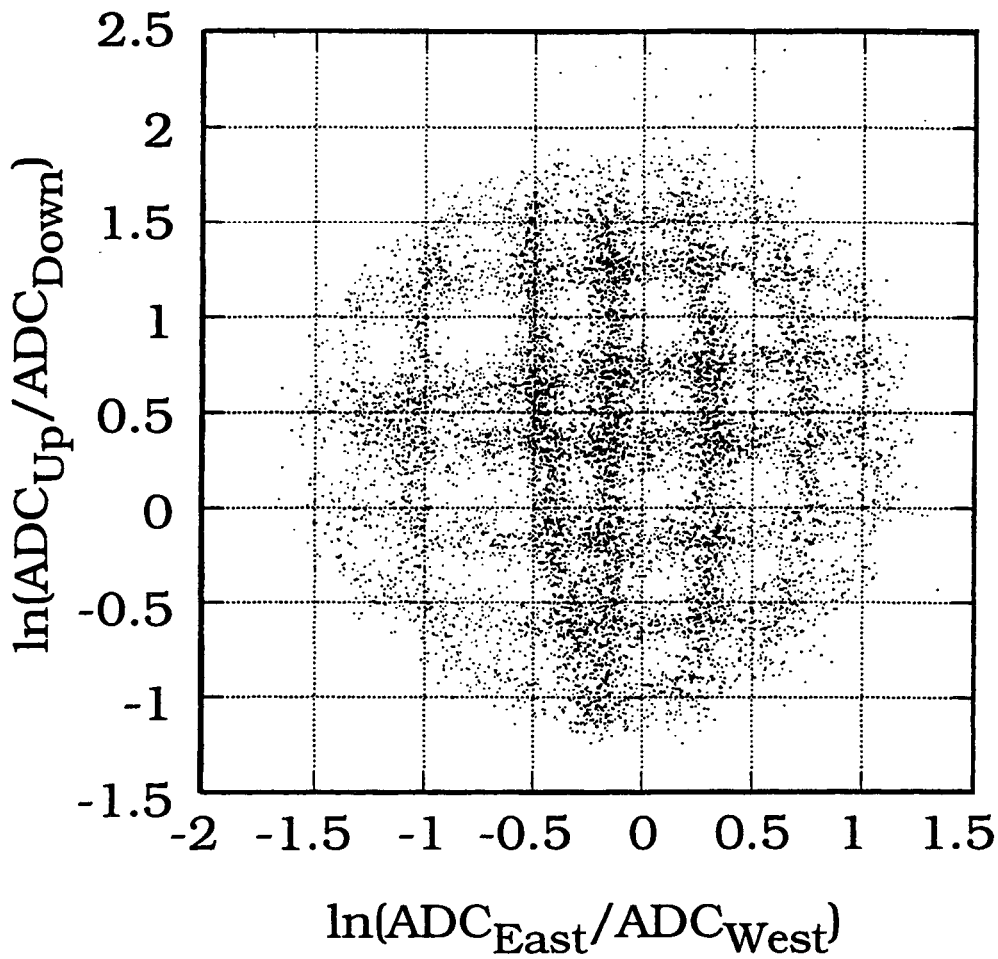
Figure 14:From track orientation inside the DC (top) to "pseudo" rigidity (center) and "pseudo" mass (bottom) of the oxygen fragments produced by ^{22}Ne at 581 A MeV.
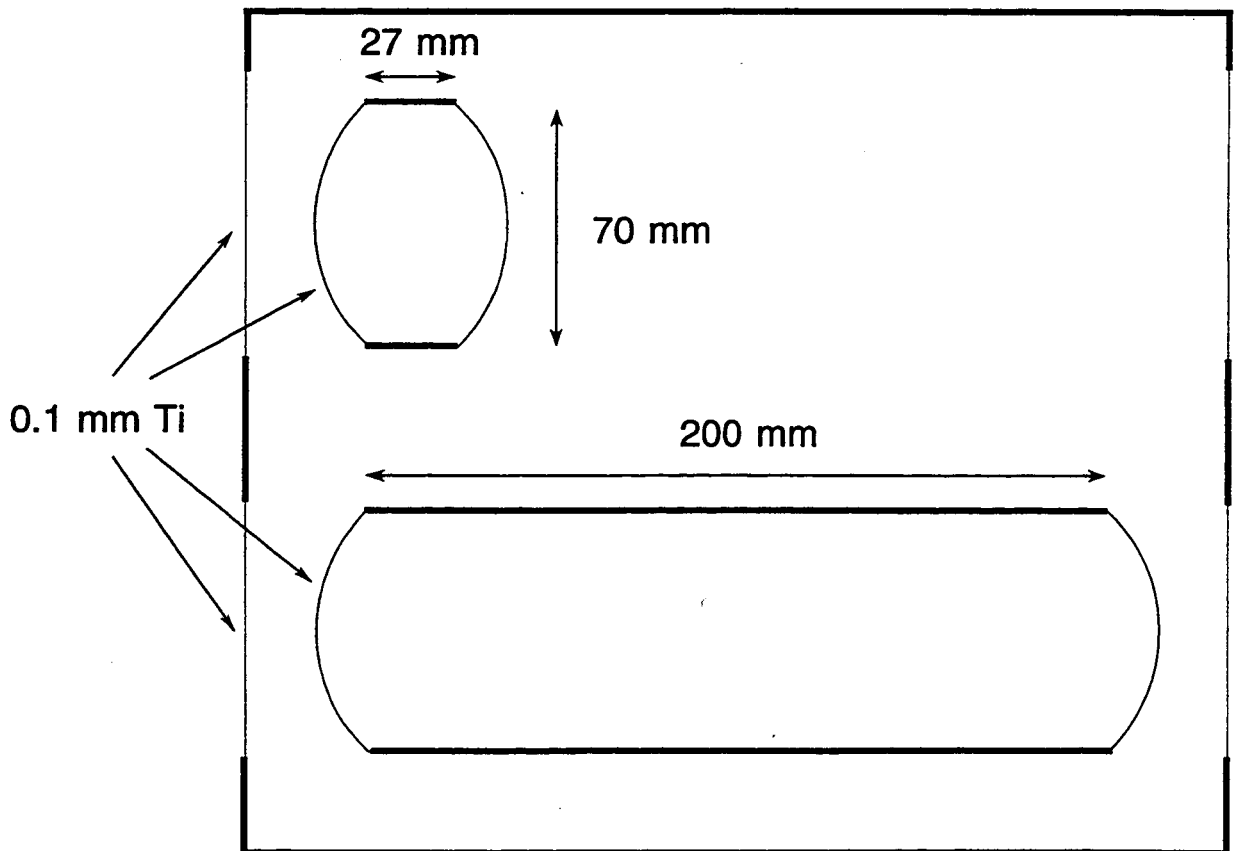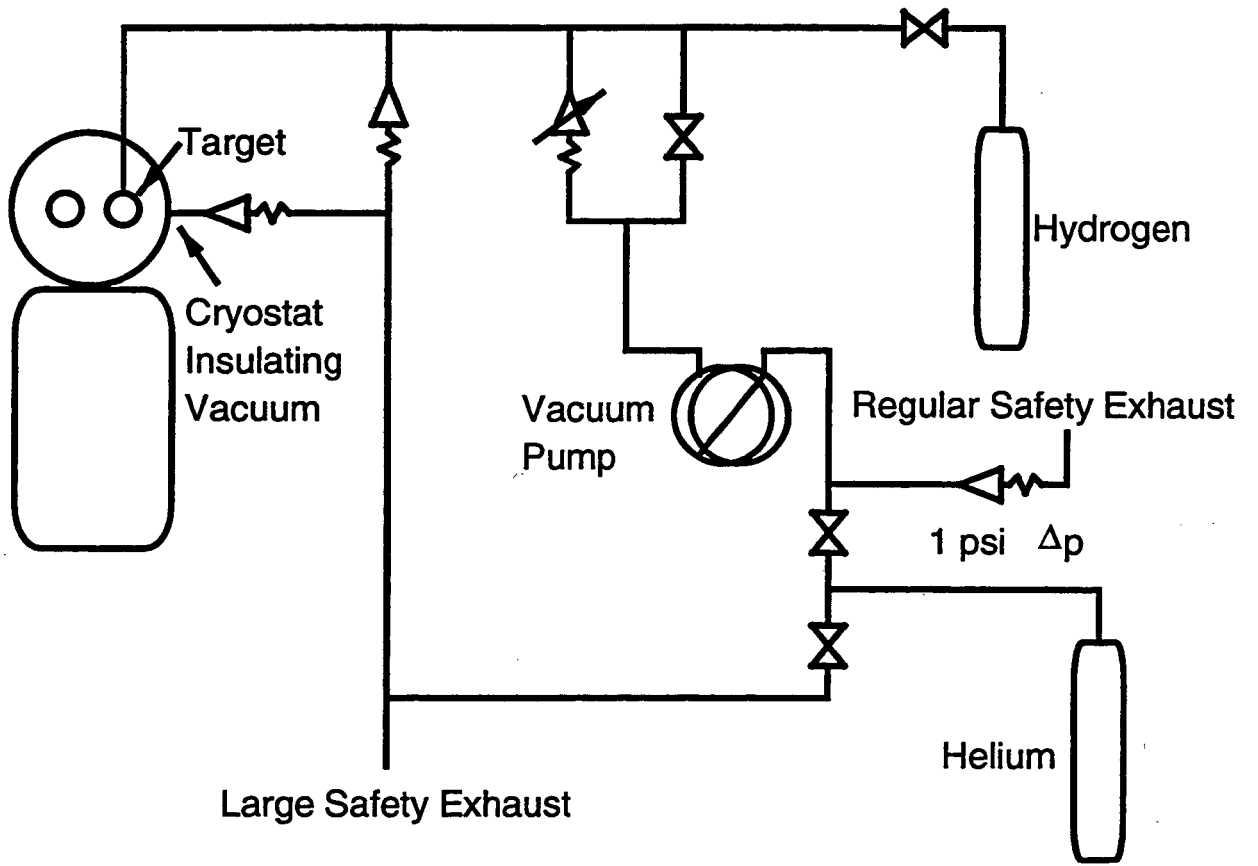
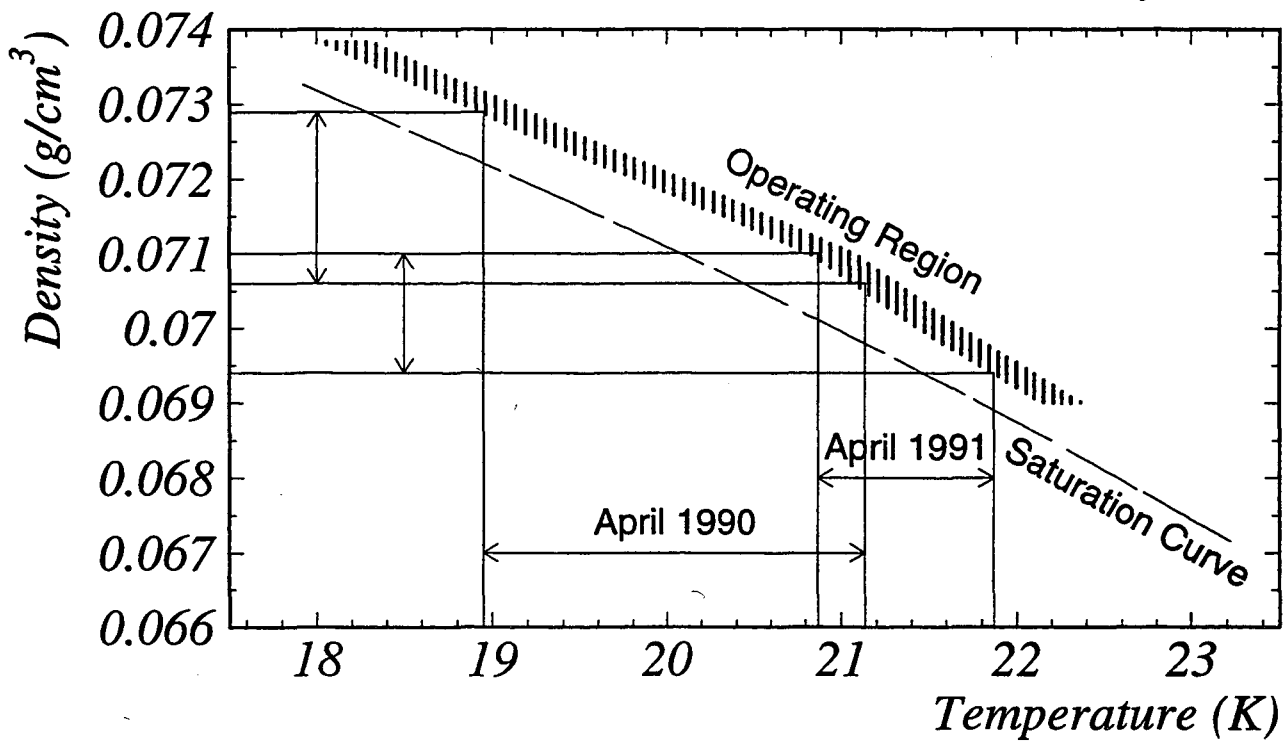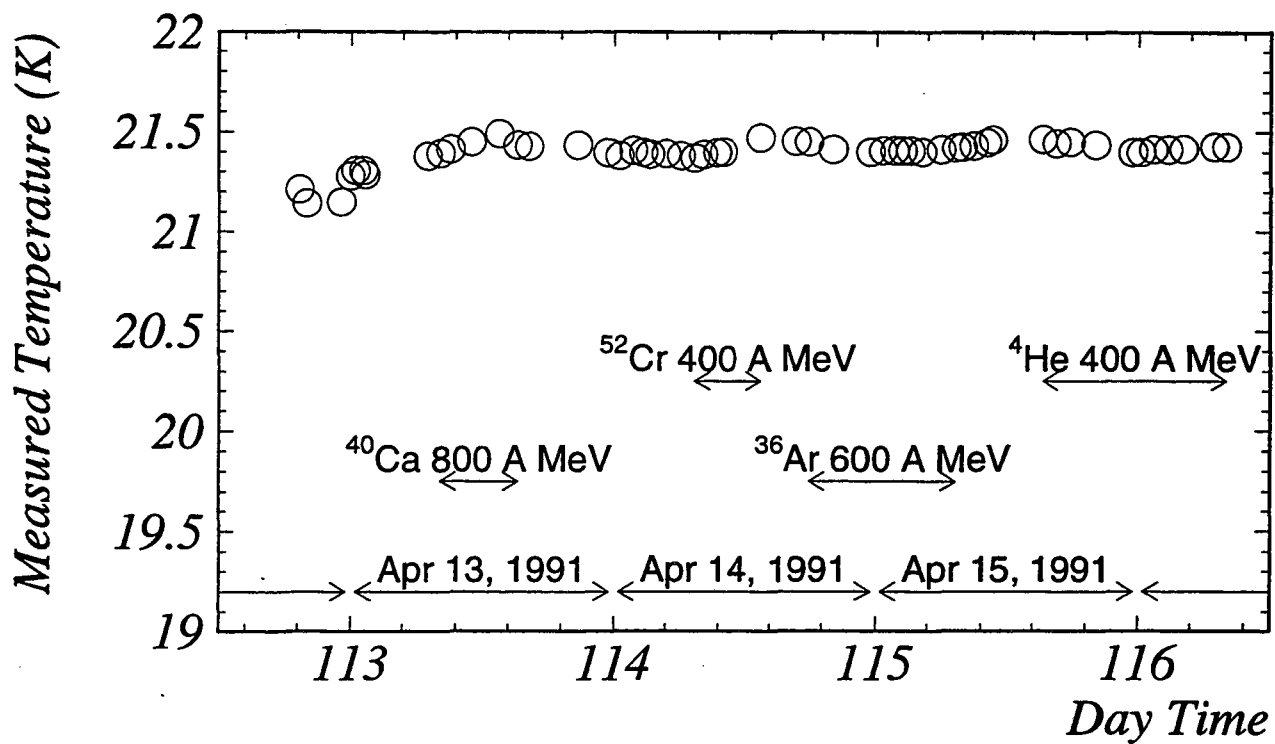Figure 15:Mass histograms for the events shown in figure 14.

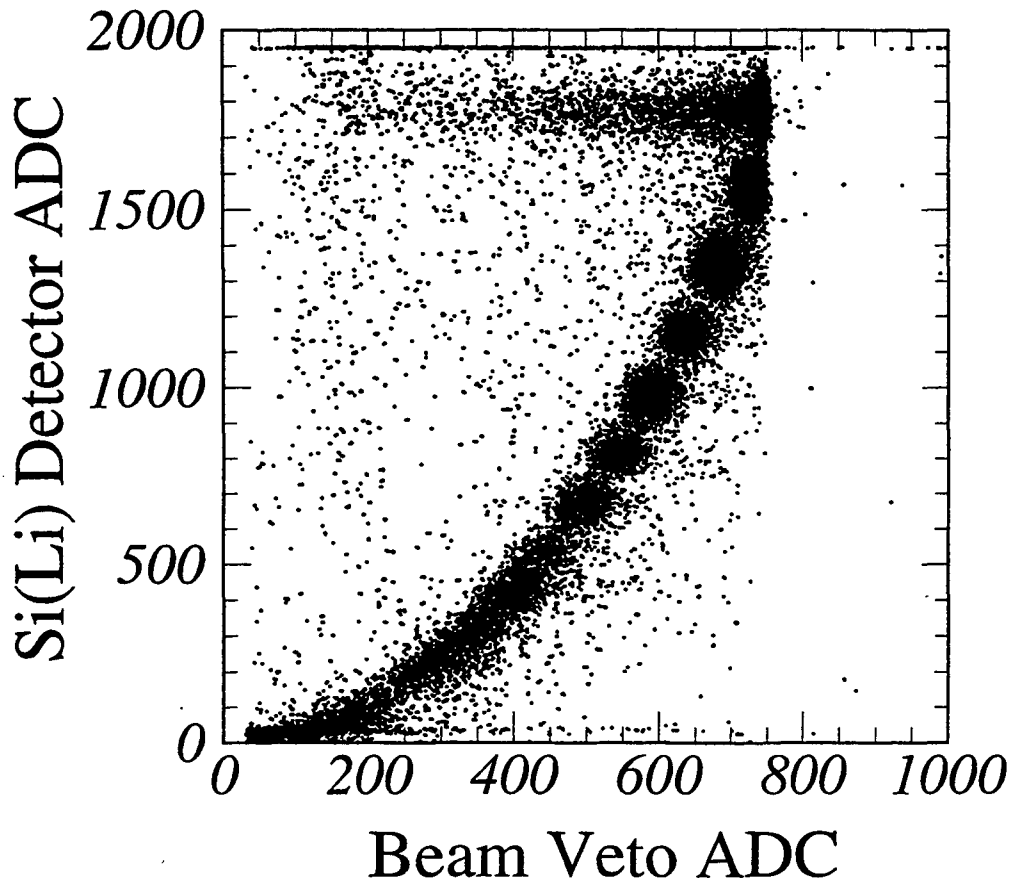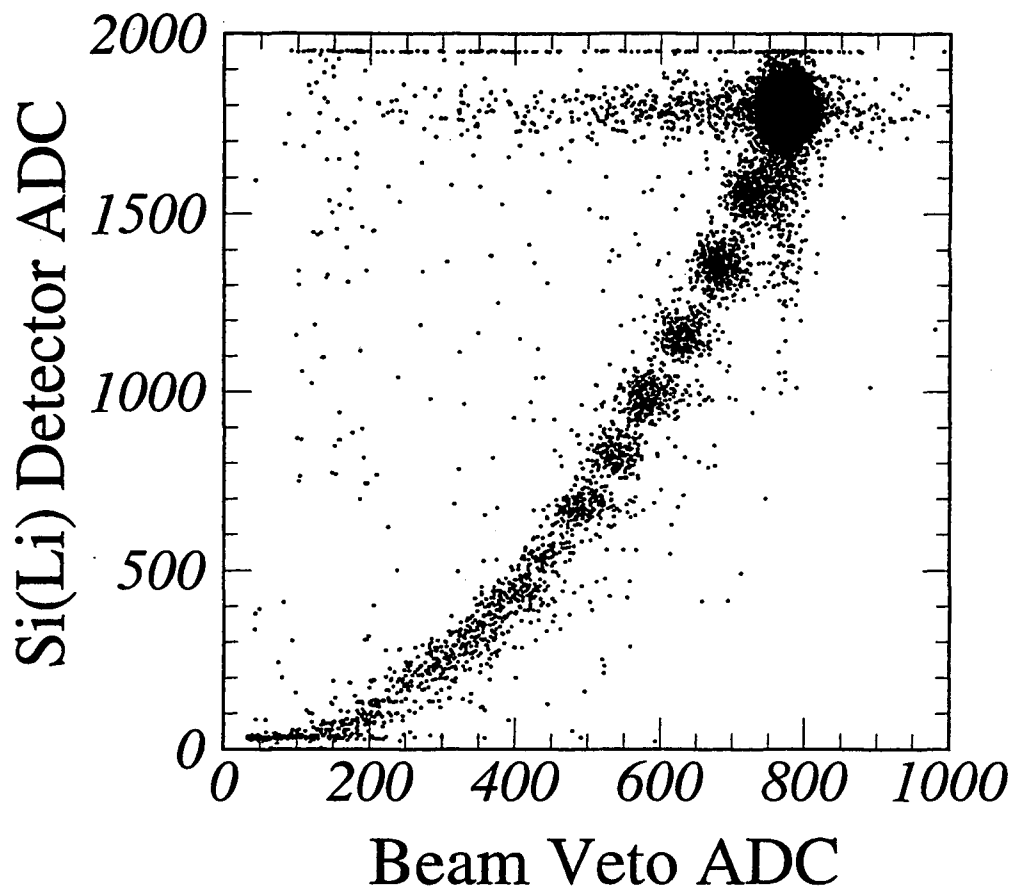S1V1

PSD

HISS

TOF

TGT FISH

MUFFINS

AV

SSD
BV

S2V2

1m

22°

Drift
Chamber

VMD

TOF
WALL

Quad Q3C

WC5

S1 V1

Beam

WC6

PSD1

AV   WC7

PSD2 S2V2

TGT

SSD
V4

BV FISH

-10   -2   -1   0   1m

40

Target

Cryostat
Insulating
Vacuum

Vacuum
Pump

Hydrogen

Regular Safety Exhaust

1 psi Δp

Helium

Large Safety Exhaust

27 mm

70 mm

0.1 mm Ti

200 mm

```
                          ┌─────────────────┐
                          │    Raw data     │
                          │  Clean / Archive│
                          └─────────────────┘
                    ┌──────────────┴──────────────────────────────┐
                    │                                              │
          ┌─────────────────┐                          ┌─────────────────┐
          │    Upstream     │                          │   Downstream    │
          │   Data Subset   │                          │   Data Subset   │
          └─────────────────┘                          └─────────────────┘
        ┌─────────┼──────────┐                                  │
  ┌──────────┐┌──────────┐┌──────────┐                   ┌─────────────┐
  │   Beam   ││Diagnostic││ BV, SSD  │                   │     DC      │
  │  Vector  ││  Plots   ││  Charge  │                   │ Calibration │
  └──────────┘└──────────┘└──────────┘                   └─────────────┘
  ┌──────────┐┌──────────┐                                     │
  │  Target  ││   Beam   │                              ┌─────────────┐
  │Thickness ││Definition│                              │   DC, TOF   │
  └──────────┘└──────────┘          ┌─────────────┐     │  pointing   │
  ┌──────────┐                      │   Level 1   │←────└─────────────┘
  │ Upstream │                      │ Processing  │            │
  │Acceptance│                      └─────────────┘     ┌─────────────┐
  └──────────┘                             │            │TOF Position │
 ┌───────────────────┐                     │            │     Map     │
 │ Charge Changing   │                     │            └─────────────┘
 │  Cross Sections   │                     │                   │
 └───────────────────┘              ┌─────────────┐     ┌─────────────┐
                                    │  Level 2a   │←────│   TOF Z,T   │
                                    │ Processing  │     │ Calibration │
                                    └─────────────┘     └─────────────┘
              ┌─────────────┐              │      ┌─────────────┐
              │  Absolute   │              │      │ Pseudo-R, M │
              │  Rigidity   │              │      │ Calibration │
              └─────────────┘              │      └─────────────┘
  ┌─────────────┐       │          │       │             │
  │    FISH     │       │    ┌─────────────┐      ┌─────────────┐
  │ Calibration │       └───→│  Level 2c   │      │  Level 2b   │←─────┘
  └─────────────┘────────────│ Processing  │      │ Processing  │
                             └─────────────┘      └─────────────┘
                                                         ┌─────────────┐
                                                         │ Downstream  │
                                                         │ Acceptance  │
  ┌─────────────┐     ┌─────────────┐     ┌─────────────┐└─────────────┘
  │    Data     │────→│   Isotope   │←────│ Background  │←────┘
  │  Selection  │     │   Yeilds    │     │ Corrections │
  └─────────────┘     └─────────────┘     └─────────────┘
                     ┌─────────┴──────────┐
          ┌─────────────────┐    ┌─────────────────┐
          │    Momentum     │    │    Isotope      │
          │  Distibutions   │    │ Cross Sections  │
          └─────────────────┘    └─────────────────┘
```
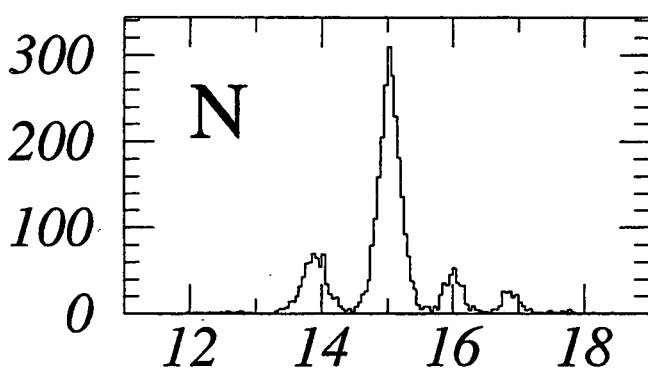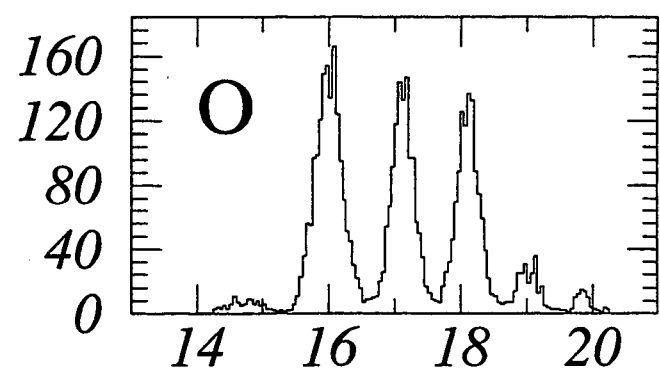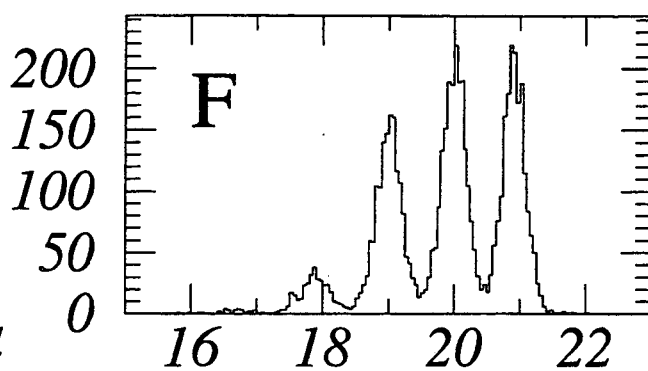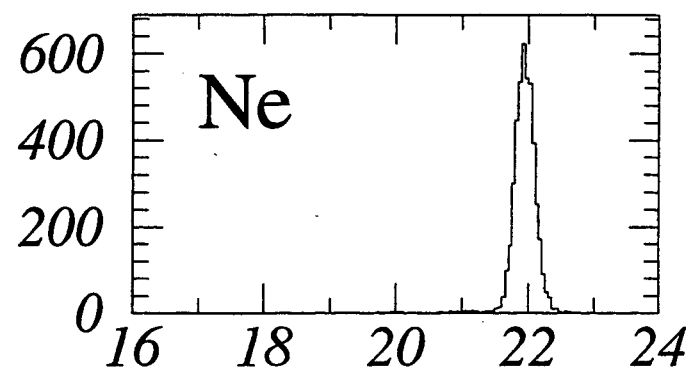
$^{22}Ne + H \longrightarrow O$

ERNEST ORLANDO LAWRENCE BERKELEY NATIONAL LABORATORY
ONE CYCLOTRON ROAD | BERKELEY, CALIFORNIA 94720